# The flow between two finite rotating disks enclosed by a cylinder

By D. DIJKSTRA AND G. J. F. VAN HEIJST†

Department of Applied Mathematics, Twente University of Technology,
Enschede, The Netherlands

The flow between two finite rotating disks enclosed by a cylinder is investigated both numerically and experimentally. For this finite geometry the full stationary Navier–Stokes equations are solved numerically without similarity assumptions. Experimental results are obtained by means of stereophotography of small tracer particles. The results are in good agreement with the numerical solution. Owing to the presence of the cylinder sidewall, the solution is found to be unique for all values of the parameters considered. When the disks rotate in opposite senses with counter-rotation above 15 %, a stagnation point appears at the slower-rotating disk. This stagnation point is associated with a two-cell structure in the meridional plane and is experimentally observed as a ring of particles at the slower-rotating disk. Near the axis of rotation the solution is found to satisfy similarity demands; for weak counter-rotation the solution is of Batchelor type near the axis of rotation, but for strong counter-rotation a Stewartson profile is found to be more adequate for the description of the tangential velocity near the axis.

## 1. Introduction

The steady flow of an incompressible viscous fluid between two infinite rotating disks has aroused considerable interest because it offers the possibility of obtaining exact solutions of the Navier–Stokes equations.

Von Kármán (1921) investigated the flow above a single infinite rotating disk; he showed that the Navier–Stokes equations can be reduced to a set of nonlinear ordinary differential equations by means of a similarity transformation. Von Kármán pointed out that outside the disk-boundary layer the tangential and radial velocities tend to zero for increasing Reynolds number.

Batchelor (1951) showed that, on the basis of von Kármán's similarity transformation, the single-disk problem could be extended to the flow between two rotating disks. He argued that for high Reynolds numbers the main body of the fluid would rotate with constant angular velocity, and that boundary layers would develop at both disks. Investigating the same problem, Stewartson (1953) prediced that, for the case of counter-rotating disks as well as with one disk at rest, the main body of the fluid outside the disk-boundary layers would not rotate. This is in contrast with Batchelor's suggestion. Picha & Eckert (1958) confirmed Stewartson's conclusions experimentally for the case of counter-rotating disks. They brought out the importance of the housing of the disks. In particular with one disk at rest, they found a Batchelor type of flow with housing, whereas a Stewartson flow was found when the disks are free.

† Department of Applied Physics, Twente University of Technology, Enschede, The Netherlands.

Some years later, Mellor, Chapple & Stokes (1968) reported the so-called multiple-cell solutions obtained by numerical techniques (here a cell is defined by planes parallel to the disks at which the vertical velocity vanishes). They treated the problem when one disk is rotating while the other is stationary, and discovered two one-cell branches, one two-cell branch and one three-cell branch of solutions.

Roberts & Shipman (1976) confirmed and extended the work of Mellor *et al.* and produced five-cell solutions. The first of the one-cell branches corresponds to the set of solutions discussed by Batchelor (1951); the other branch leads in the limit of large Reynolds numbers to the single-disk solution of von Kármán (1921).

Nguyen, Ribault & Florent (1975) also established the existence of multiple solutions: for a given flow configuration several solutions appear to exist. At moderate Reynolds numbers a Batchelor-type solution is found, at higher Reynolds numbers an additional (Stewartson-type) solution is obtained numerically.

This work has been extended by Holodniok, Kubicek & Hlavacek (1977); for the case $s = 0.8$ ($s = \Omega_T/\Omega_B$ is the ratio of the angular velocities of the top and bottom disks) they found branches of one, three and even five solutions. Some of those branches contained Batchelor-type as well as Stewartson-type solutions. Later on, Holodniok, Kubicek & Hlavacek (1981) computed a multiplicity of similarity solutions in the range $-1 \leqslant s \leqslant 1$ at $Re = 625$. Non-unique solutions to the *single-disk* problem have been calculated by Zandbergen & Dijkstra (1977). Later on, Zandbergen (1979) and Dijkstra (1980) showed that the original von Kármán problem of a rotating disk in an infinite stationary medium has an infinite number of solutions.

All papers referred to above are based on the similarity equations, but for disks confined in a circular cylinder the *partial* differential equations must be used for the description of the flow.

Pao (1970, 1972) investigated the flow between two finite disks confined in a cylinder of aspect ratio 1. He obtained solutions of the full stationary Navier–Stokes equations for the case where one of the disks is held fixed. When the Reynolds number is increased beyond 400 his numerical procedure did not converge anymore.

Lugt & Haussling (1973) extended Pao's work and obtained numerical results for one disk fixed ($s = 0$) and Ekman numbers down to 0.0002. For the case of counter-rotating disks ($s < 0$) they calculated results at $Ek = 0.01$ and established a two-cell structure in the meridional plane for certain negative values of $s$.

During the past decades a lot of numerical work has been done, but experimental verifications of numerical results are scarce, in particular for the case where the disks are rotating in opposite senses.

Mellor *et al.* (1968) and Nguyen *et al.* (1975) used a hot-wire anemometer to measure the tangential and radial velocity components of the flow between two finite disks of which one is rotating. Although edge effects appeared to be considerable, the experimental results corresponded to a Batchelor-type flow.

For the confined arrangement with one stationary and one rotating disk, tangential velocity measurements were performed by Bien & Penner (1970), using a laser-Doppler anemometer. They too indicated the presence of a Batchelor-type flow: far from the cylinder sidewall the main body of the fluid appeared to rotate.

Concerning the flow between two disks, most experiments known thus far have been carried out for a stationary and a rotating disk. In the present study we investigate the fluid flow between two finite rotating disks confined in a cylinder of low aspect ratio for general rotation ratios $s$, at Reynolds numbers varying from 100 to 1000. The most interesting results are obtained for negative values of $s$, so that the main part of this work focuses attention on the counter-rotation case.
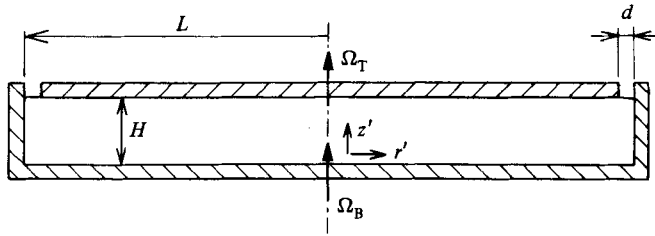
FIGURE 1. The geometry of the problem.

For this finite geometry the full Navier–Stokes equations have been solved numerically using a finite-difference technique. When one disk is stationary ($s = 0$), solutions are obtained for Reynolds numbers up to 1000. When the disks rotate in opposite senses ($s < 0$) the numerical iteration still converges for Reynolds numbers up to 100, producing extremely interesting solutions, similar to those reported by Lugt & Haussling (1973). The flow in the meridional plane appears to possess a two-cell character: the shape of the cells depends on the rotation ratio $s$ and the Reynolds number. A *stagnation point* occurs on the slowest rotating disk.

Experimental results were obtained, using a measuring technique based on stereophotography of small tracer particles in the fluid. At the stagnation point these tracer particles crowd together, producing a ring (at the slowest rotating disk) which is clearly observable. The numerical and the experimental results perfectly agree for both the position of the stagnation point and the velocity components elsewhere in the fluid. However, multiple solutions have not been found, either experimentally, or numerically.

## 2. Formulation of the problem

In order to model the flow between two infinite rotating disks we consider a rotating cylinder with small aspect ratio $\delta = H/L$ ($H$ and $L$ denoting respectively the height and radius of the cylinder, see figure 1), filled with a homogeneous, slightly viscous Newtonian fluid with kinematic viscosity $\nu$ and constant density $\rho$. The top and bottom disks of the cylinder can rotate independently with constant angular velocities $\Omega_T$ and $\Omega_B$ respectively.

For a convenient description of the flow it is useful to define the ratio of angular velocities as

$$s = \Omega_T/\Omega_B. \tag{2.1}$$

The sidewall of the cylinder is fixed to the bottom disk, and consequently rotates with angular velocity $\Omega_B$ as well. The case $s = 1$ corresponds to solid-body rotation and will be excluded in the sequel. It is assumed that the flow in the cylinder is laminar and stationary.

The motion of the fluid (velocity components $u', v', w'$) will be related to a non-rotating cylindrical coordinate system $(r', \theta, z')$. It is convenient to non-dimensionalize the coordinates, the velocity components and the pressure $p'$ as follows:

$$\left.\begin{aligned}
r' &= rL, \quad u' = uL\Delta\Omega, \quad p' = p\rho L^2\Delta\Omega\,\Omega_{max}, \\
z' &= zH, \quad v' = vL\Delta\Omega, \quad w' = wH\Delta\Omega, \\
\Delta\Omega &= |\Omega_B - \Omega_T|, \quad \Omega_{max} = \max(|\Omega_B|, |\Omega_T|),
\end{aligned}\right\} \tag{2.2}$$

where prime quantities are dimensional. By symmetry, the equations of momentum (Navier–Stokes) and continuity then take the following non-dimensional forms:

$$Ro\left(u\frac{\partial u}{\partial r}+w\frac{\partial u}{\partial z}-\frac{v^2}{r}\right)=-\frac{\partial p}{\partial r}+Ek\left[\delta^2\left(\frac{\partial^2 u}{\partial r^2}+\frac{1}{r}\frac{\partial u}{\partial r}-\frac{u}{r^2}\right)+\frac{\partial^2 u}{\partial z^2}\right],\qquad(2.3)$$

$$Ro\left(u\frac{\partial v}{\partial r}+w\frac{\partial v}{\partial z}+\frac{uv}{r}\right)=Ek\left[\delta^2\left(\frac{\partial^2 v}{\partial r^2}+\frac{1}{r}\frac{\partial v}{\partial r}-\frac{v}{r^2}\right)+\frac{\partial^2 v}{\partial z^2}\right],\qquad(2.4)$$

$$Ro\left(u\frac{\partial w}{\partial r}+w\frac{\partial w}{\partial z}\right)=-\frac{1}{\delta^2}\frac{\partial p}{\partial z}+Ek\left[\delta^2\left(\frac{\partial^2 w}{\partial r^2}+\frac{1}{r}\frac{\partial w}{\partial r}\right)+\frac{\partial^2 w}{\partial z^2}\right],\qquad(2.5)$$

$$\frac{u}{r}+\frac{\partial u}{\partial r}+\frac{\partial w}{\partial z}=0,\qquad(2.6)$$

with the non-dimensional parameters

$$\left.\begin{aligned}Ro &=\frac{\Delta\Omega}{\Omega_{max}}\quad\text{(Rossby number)},\\[2mm]Ek &=\frac{\nu}{H^2\Omega_{max}}\quad\text{(Ekman number)},\\[2mm]\delta &=\frac{H}{L}\quad\text{(aspect ratio)}.\end{aligned}\right\}\qquad(2.7)$$

It is common to use the Reynolds number $Re^*$ defined by

$$Re^*=\frac{1}{Ek}=\frac{H^2\Omega_{max}}{\nu}.\qquad(2.8)$$

The (non-dimensional) boundary conditions for the basic equations (2.3)–(2.6) are (see figure 1):

$$\left.\begin{aligned}u &=0,\quad v=ar,\quad w=0\quad(z=0,\quad 0\leqslant r\leqslant 1),\\u &=0,\quad v=sar,\quad w=0\quad(z=1,\quad 0\leqslant r\leqslant 1),\\u &=0,\quad v=a,\quad w=0\quad(r=1,\quad 0\leqslant z\leqslant 1),\end{aligned}\right\}\qquad(2.9)$$

with $a=\Omega_B/\Delta\Omega$.

The axisymmetry of the problem permits a description in terms of the meridional stream function $\psi$ and the azimuthal component $\zeta$ of the vorticity vector, defined by

$$u=\frac{1}{r}\frac{\partial\psi}{\partial z},\quad w=-\frac{1}{r}\frac{\partial\psi}{\partial r},\quad\zeta=\frac{\partial u}{\partial z}-\delta^2\frac{\partial w}{\partial r}.\qquad(2.10)$$

By elimination of the pressure $p$, the governing equations (2.3)–(2.6) can then be written as

$$Ro\left(u\frac{\partial v}{\partial r}+w\frac{\partial v}{\partial z}+\frac{uv}{r}\right)=Ek\left[\delta^2\left(\frac{\partial^2 v}{\partial r^2}+\frac{1}{r}\frac{\partial v}{\partial r}-\frac{v}{r^2}\right)+\frac{\partial^2 v}{\partial z^2}\right],\qquad(2.11)$$

$$Ro\left(u\frac{\partial\zeta}{\partial r}+w\frac{\partial\zeta}{\partial z}-\frac{u\zeta}{r}-\frac{2v}{r}\frac{\partial v}{\partial z}\right)=Ek\left[\delta^2\left(\frac{\partial^2\zeta}{\partial r^2}+\frac{1}{r}\frac{\partial\zeta}{\partial r}-\frac{\zeta}{r^2}\right)+\frac{\partial^2\zeta}{\partial z^2}\right],\qquad(2.12)$$

$$r\zeta=\delta^2\left(\frac{\partial^2\psi}{\partial r^2}-\frac{1}{r}\frac{\partial\psi}{\partial r}\right)+\frac{\partial^2\psi}{\partial z^2}.\qquad(2.13)$$

Expressed in terms of $v$, $\psi$ and $\zeta$, the boundary conditions (2.9) become, with $a = \Omega_{\mathrm{B}}/\Delta\Omega$,

$$\left.\begin{aligned}
\frac{\partial\psi}{\partial z} &= 0, \quad v = ar, \quad \psi = 0 \quad (z = 0, \quad 0 \leqslant r \leqslant 1), \\[2mm]
\frac{\partial\psi}{\partial z} &= 0, \quad v = sar, \quad \psi = 0 \quad (z = 1, \quad 0 \leqslant r \leqslant 1), \\[2mm]
\frac{\partial\psi}{\partial r} &= 0, \quad v = a, \quad \psi = 0 \quad (r = 1, \quad 0 \leqslant z \leqslant 1), \\[2mm]
\zeta &= 0, \quad v = 0, \quad \psi = 0 \quad (r = 0, \quad 0 \leqslant z \leqslant 1).
\end{aligned}\right\} \tag{2.14}$$

The latter condition at $r = 0$ is a consequence of the axisymmetry in the flow configuration.

In reality, a narrow gap of width $d$ is present between the upper disk and the cylinder sidewall (see figure 1); in this gap the fluid has a free surface, which is throughout assumed to be flat. For an adequate description of the flow near the gap, the boundary condition (2.14) at $z = 1$ must be replaced by

$$\left.\begin{aligned}
\frac{\partial\psi}{\partial z} &= 0, \quad v = sar, \quad \psi = 0 \quad \left(z = 1, \quad 0 \leqslant r \leqslant 1 - \frac{d}{L}\right), \\[2mm]
\frac{\partial\psi}{\partial z} &= 0, \quad v = l(r), \quad \psi = 0 \quad \left(z = 1, \quad 1 - \frac{d}{L} \leqslant r \leqslant 1\right),
\end{aligned}\right\} \tag{2.15}$$

in which $l(r)$ is some function of the radial coordinate. In the numerical part of this study (§3) $l(r)$ is considered to be linear in $r$.

## 3. The numerical method of solution

### 3.1. *General outline of the method*

The full system (2.11)–(2.13) of partial differential equations with boundary conditions (2.14) has been solved by means of a finite-difference technique using central differencing. The first-order derivatives appearing in the nonlinear part of (2.11) and (2.12) are discretized in two ways, central or upwind differencing, leading to two modes of the final computer program. For the sake of resolution near the walls, coordinate-stretching functions are introduced. The discretizations are performed with a uniform grid in the transformed plane; the resulting system of nonlinear algebraic equations is solved by means of an alternating-direction implicit (ADI) technique and Newton iteration to cope with nonlinearity.

### 3.2. *Transformation of independent variables and equations*

For small values of the Ekman number $Ek$ we may expect boundary layers at the disks and also at the cylinder sidewall. In order to obtain sufficient resolution of the numerical method in these layers a coordinate transformation is applied. This approach is similar to that adopted by Lugt & Haussling (1973), although we will use other stretching functions. The present transformation of the radial coordinate $r$ and the axial coordinate $z$ is taken as follows:

$$x = X(r) = \frac{\exp(\alpha r) - 1}{\exp(\alpha) - 1}, \quad \alpha > 0, \tag{3.1}$$

$$y = Y(z) = \frac{z(1 + \beta\epsilon)}{2(z + \beta\epsilon)} + \frac{z\gamma\epsilon}{2(1 - z + \gamma\epsilon)}, \quad \epsilon = \left(\frac{Ek}{Ro}\right)^{\frac{1}{2}}, \quad \beta > 0, \quad \gamma > 0. \tag{3.2}$$

Since $X'$ and $Y'$ are positive-definite and $X(0) = Y(0) = 0$, $X(1) = Y(1) = 1$, this transformation maps the region $0 \leqslant r, z \leqslant 1$ onto the region $0 \leqslant x, y \leqslant 1$ in a monotonic and uniquely invertible way. The inverse functions will be denoted by

$$r = R(x) \equiv X^{-1}(x), \quad z = Z(y) \equiv Y^{-1}(y). \tag{3.3}$$

The parameter $\epsilon$ in (3.2) is a measure for the thickness of the boundary layers at the disks. Note that the two pole singularities in (3.2) are at $z = -\beta\epsilon$ and at $z = 1 + \gamma\epsilon$, both at a distance $O(\epsilon)$ outside the interval $0 \leqslant z \leqslant 1$. The value of $\epsilon$ will be small and prescribed for a given problem. In contrast with $\epsilon$ the parameters $\alpha$, $\beta$ and $\gamma$ appearing in the transformation are numerical control parameters, chosen in such a way that the transformation has the desired effect, i.e. to produce mesh points where required (see §3.3). In the final production stage of the numerical work the following values for the transformation parameters have been used:

$$\begin{aligned} \alpha = 3, \quad \beta = \gamma = 2 \quad (0 < Ek < 0.01), \\ \alpha = 3, \quad \beta = \gamma = \infty \quad (Ek \geqslant 0.01). \end{aligned} \Bigg\} \tag{3.4}$$

It is easy to see that in the limit $\beta, \gamma \to \infty$ the axial transformation (3.2) reduces to the identity $Y(z) \equiv z$, in other words no axial transformation is applied for $Ek \geqslant 0.01$ (and Rossby numbers $Ro$ of order unity).

We now consider the transformation of (2.11)–(2.13). In terms of the new coordinates $x$ and $y$ defined above, the system is written in the following compact form:

$$Ro\left(J + \frac{u}{r}\right)v = Ek\left(L - \frac{\delta^2}{r^2}\right)v, \tag{3.5}$$

$$Ro\left[\left(J - \frac{u}{r}\right)\zeta - Kv\right] = Ek\left(L - \frac{\delta^2}{r^2}\right)\zeta, \tag{3.6}$$

$$r\zeta = (L - M)\psi, \tag{3.7}$$

where

$$J = u\frac{\partial}{\partial r} + w\frac{\partial}{\partial z} = \frac{1}{R(x)\,R'(x)\,Z'(y)}\left(\frac{\partial\psi}{\partial y}\frac{\partial}{\partial x} - \frac{\partial\psi}{\partial x}\frac{\partial}{\partial y}\right), \tag{3.8}$$

$$K = \frac{2}{r}v\frac{\partial}{\partial z} = \frac{2v}{R(x)\,Z'(y)}\frac{\partial}{\partial y}, \tag{3.9}$$

$$\begin{aligned} L &= \delta^2\left(\frac{\partial^2}{\partial r^2} + \frac{1}{r}\frac{\partial}{\partial r}\right) + \frac{\partial^2}{\partial z^2} \\ &= \frac{\delta^2}{R'^2(x)}\left[\frac{\partial^2}{\partial x^2} + \left\{\frac{R'(x)}{R(x)} - \frac{R''(x)}{R'(x)}\right\}\frac{\partial}{\partial x}\right] + \frac{1}{Z'^2(y)}\left(\frac{\partial^2}{\partial y^2} - \frac{Z''(y)}{Z'(y)}\frac{\partial}{\partial y}\right), \end{aligned} \tag{3.10}$$

$$M = \frac{2\delta^2}{r}\frac{\partial}{\partial r} = \frac{2\delta^2}{R(x)\,R'(x)}\frac{\partial}{\partial x}, \tag{3.11}$$

$$r = R(x), \quad u = \frac{1}{r}\frac{\partial\psi}{\partial z} = \frac{1}{R(x)\,Z'(y)}\frac{\partial\psi}{\partial y}. \tag{3.12}$$

The functions $R(x)$ and $Z(y)$ are given by (3.3), and the velocity components $u$ and $w$ have been written in terms of the stream function $\psi$, (2.10). The boundary

conditions in the transformed plane become

$$
\left.\begin{aligned}
\frac{\partial \psi}{\partial y} = 0, \quad v = aR(x), \quad \psi = 0 \quad (y = 0, \quad 0 \leqslant x \leqslant 1), \\[2mm]
\frac{\partial \psi}{\partial y} = 0, \quad v = saR(x), \quad \psi = 0 \quad (y = 1, \quad 0 \leqslant x \leqslant 1), \\[2mm]
\frac{\partial \psi}{\partial x} = 0, \quad v = a, \quad \psi = 0 \quad (x = 1, \quad 0 \leqslant y \leqslant 1), \\[2mm]
\zeta = 0, \quad v = 0, \quad \psi = 0 \quad (x = 0, \quad 0 \leqslant y \leqslant 1),
\end{aligned}\right\}
\tag{3.13}
$$

with $a = \Omega_{\mathrm{B}}/\Delta\Omega$. The discretization of the transformed system will be considered in §3.3.

### 3.3. *Discrete approach*

In the transformed plane the region of calculation is the unit square $0 \leqslant x, y \leqslant 1$, which is covered by a uniform grid with mesh points $(x_i, y_j)$:

$$
\left.\begin{aligned}
x_i = i\Delta x, \quad y_j = j\Delta y, \quad i = 0(1)\,N_x, \quad j = 0(1)\,N_y, \\[2mm]
\Delta x = \frac{1}{N_x}, \quad \Delta y = \frac{1}{N_y}.
\end{aligned}\right\}
\tag{3.14}
$$

The majority of the calculations has been performed with $N_x = N_y = 20$ (441 mesh points). When considered in the original $(r, z)$-plane the grid may be highly non-uniform, depending on the values of the parameters in the transformation (3.1)–(3.2). To illustrate this we consider the case where the top disk is stationary ($s = 0$, $Ro = 1$) and $Ek = 0.001$. With control parameters given by (3.4) it is found that each disk boundary layer contains about 30 % of the axial grid points – see figure 16 in the appendix for a graphical representation. As for the radial mesh one finds that with $N_x = 20$ the first interior mesh point has an $r$-coordinate $r_1 = 0.2233$, while the last interior radial point is at $r_{19} = 0.9838$. The need of a concentration of mesh points near $r = 1$ follows from the fact that in general radial gradients are much larger near $r = 1$ than near $r = 0$, where the solution is of von Kármán similarity type (see appendix, figure 17).

On the grid defined above we now consider the discretization of the governing equations (3.5)–(3.12). Two different discretizations have been employed, viz central and upwind differencing. In the central mode all derivatives in the governing equations are replaced by central differences, e.g.

$$
\frac{\partial T}{\partial x} = \frac{T_{i+1,j} - T_{i-1,j}}{2\Delta x}, \quad \frac{\partial^2 T}{\partial x^2} = \frac{T_{i+1,j} - 2T_{ij} + T_{i-1,j}}{\Delta^2 x},
\tag{3.15}
$$

and similarly for the derivatives with respect to $y$. The quantity $T_{ij}$ symbolizes the three unknowns $v$, $\zeta$ and $\psi$ at mesh point $(x_i, y_j)$.

In the upwind mode, upwind differencing is used to replace the first-order derivatives of $v$ and $\zeta$ appearing in $J(v)$ and $J(\zeta)$, (3.5) and (3.6) respectively; all other derivatives in the system (including derivatives of $\psi$ appearing in $J$) are replaced by central-difference quotients. The differencing of $J$ depends on the signs of the velocity components $u$ and $w$ in the usual way, e.g. $\partial/\partial x$ is replaced by a one-sided backward-

(forward-) difference quotient if $u > 0$ ($u < 0$), and similarly for $\partial/\partial y$, depending on sgn $(w)$. An example is

$$J(\zeta) = \frac{1}{R(x_i)\,R'(x_i)\,Z'(y_j)}\left[\frac{\psi_{i,j+1}-\psi_{i,j-1}}{2\Delta y}\frac{\zeta_{i,j}-\zeta_{i-1,j}}{\Delta x}-\frac{\psi_{i+1,j}-\psi_{i-1,j}}{2\Delta x}\frac{\zeta_{i,j+1}-\zeta_{ij}}{\Delta y}\right]$$

$$(u > 0, \quad w < 0). \quad (3.16)$$

It is well known that upwind differencing influences the condition of the system of discrete equations in a favourable way, while the accuracy is less than in the central mode. During the initial stage of the numerical work we only considered the case $s = 0$ (top disk stationary) and the central mode appeared to behave in a satisfactory way. Later on the more difficult cases $s < 0$ (counter-rotating top disk) have been treated, and the central mode failed in the sense that the discrete solution procedure did not converge. With upwind differencing the failure was removed and converged results could be obtained.

So far, we have considered interior mesh points $(x_i, y_j)$ ($0 < i < N_x$, $0 < j < N_y$) where the discretization produces 3 algebraic equations for the unknown quantities $v_{ij}$, $\zeta_{ij}$ and $\psi_{ij}$ at each point, and we now consider the boundary conditions.

It will be clear from (3.13) that the vorticity $\zeta$ is unknown at the disks $y = 0, 1$ and at the cylinder sidewall $x = 1$. The discrete equations for the vorticity at these boundaries are obtained from (3.7) and the conditions (3.13) on the stream function $\psi$. At the bottom disk we then have

$$y = 0, \quad R(x)\,\zeta(x, 0) = \frac{1}{Z'^2(0)}\frac{\partial^2\psi}{\partial y^2}(x, 0), \left.\vphantom{\frac{1}{Z'^2(0)}}\right\}$$
$$\psi(x, 0) = \frac{\partial\psi}{\partial y}(x, 0) = 0. \qquad (3.17)$$

From Taylor expansion of $\psi(x, \Delta y)$ the discrete representation is taken as (bottom disk):

$$R(x_i)\,\zeta_{ij} - \frac{2}{\Delta^2 y Z'^2(0)}\psi_{i,j+1} = 0 \quad (j = 0, \quad 0 < i < N_x). \qquad (3.18)$$

Note that the condition $\partial\psi/\partial y = 0$ is implicitly contained in this equation. Discrete formulae for the vorticity at the top disk and the sidewall are obtained in the same way. The remaining boundary conditions (3.13) can be directly imposed, although $v$ is discontinuous at $x = y = 1$, where the top disk meets the cylinder sidewall. In the experimental arrangement (figure 2) there exists a narrow gap of width $d = 20$ mm (4% of the radius) near that point. Since the gap is small and the value of $v$ at the discontinuity does not enter into the numerical scheme we have ignored the gap during the initial stage of the investigation. Later on the boundary conditions across the gap have been replaced by (2.15). All numerical results presented in this paper have been obtained with the $(x, y)$-representation of the conditions (2.15) across the gap.

### 3.4. *Solution method of discrete equations*

The discretization presented in §3.3 results in a system of coupled nonlinear algebraic equations for the quantities $v_{ij}$, $\zeta_{ij}$ and $\psi_{ij}$. This system is solved with an alternating-direction implicit technique and Gauss–Seidel relaxation. The nonlinearity is treated by means of Newton iteration. Hence two nested iteration procedures may be distinguished in the solution method: a *global* iteration and an *inner* iteration. The organization of the global procedure is as follows.

(1) Initialize flow field.

(2) Perform axial cycle: axial($i$), $i = 1(1)N_x - 1$.

(3) Perform radial cycle: radial($j$), $j = 1(1)N_y - 1$.

(4) Test for global convergence; if not satisfied return to (2).

(5) Print solution.

Here 'axial($i$)' means that all the unknown variables (including vorticity at the disks) along grid line $i$ = constant are *simultaneously* solved by means of Newton iteration. With the results of this inner iteration the approximation to the solution along the grid line considered is then updated (after relaxation). During the axial cycle the vorticity at the sidewall is frozen. This quantity is updated during the radial cycle where now lines $j$ = constant are treated by means of radial($j$) in the same way as in the axial cycle, but this time with frozen vorticity at the disks. The execution of the axial and the radial cycle together will be called a global sweep. Upon execution of such a sweep all boundary conditions are felt by the solution over the entire domain of the calculation. The quantities at interior mesh points are updated twice during one global sweep, whereas the vorticity at disks and sidewall is updated once.

### 3.5. *Relaxation and convergence*

The Newton or inner iteration mentioned in §3.4 is ended if the maximum of the Newton corrections for all the unknown variables along the considered grid line is $< 10^{-4}$. Owing to the quadratic convergence of the Newton method this bound is small enough and it is reached with 3 iteration cycles in the initial stage of the calculation. In the final stage of the calculation the number of Newton cycles for each grid line appeared to be 1 over the entire grid, indicating that global convergence was achieved. The test on global convergence reads

$$\max_{(ij)} |T_{ij}^{(Sw)} - T_{ij}^{(Sw+\frac{1}{2})}| < 10^{-4}, \tag{3.19}$$

where $T$ stands for $v$, $\zeta$ and $\psi$, while $Sw$ and $Sw + \frac{1}{2}$ denote the axial and the radial half-sweep respectively.

To pass (3.19) underrelaxation appeared to be required depending on the Ekman number and the mode of discretization. The central mode (used for $s = 0$) required a relaxation factor $\omega = 0.5$ at $Ek = 0.01$, while $0.25$ was used at $Ek = 0.001$. The upwind mode ($s < 0$) showed a better convergence behaviour and $\omega$ could be taken more closely to 1.

### 3.6. *Checks on the numerical results*

To verify the quality of the numerical results and to test the computer program several checks are available or have been developed.

(i) *Comparison with experimental results* (§5).

(ii) *Comparison with von Kármán similarity results* (appendix).

(iii) *Grid refinement.* For some values of $s$ solutions on two grids have been computed and can be compared (§5 and appendix).

(iv) *Analytic solution at large Ekman numbers.* As $Ek \to \infty$ the solution is governed by linear equations, and the tangential velocity $v$ may be expanded in a series of Bessel functions (see Pao 1970, 1972). At an aspect ratio $\delta = 0.07$ the series of Bessel functions showed a poor convergence and hence this test has been performed with $\delta = 1$. Good agreement was obtained.

(v) *Vorticity integral.* From the definition (2.10) of the vorticity $\zeta$ it can be shown that

$$\iiint_V r\zeta \, dV = 2\pi \int_{r=0}^{1} \int_{z=0}^{1} r^2 \zeta \, dr \, dz = 0.$$

Here $V$ represents the entire volume occupied by the fluid. The vanishing of the integral over the meridional plane follows from (2.10), the boundary conditions and integration by parts. In the transformed plane the result becomes

$$\int_{x=0}^{1} \int_{y=0}^{1} R^2(x)\, \zeta(x,y)\, R'(x)\, Z'(y)\, dx\, dy = 0.$$

The discrete evaluation of the integral is performed by means of a two-dimensional trapezoidal rule where positive and negative contributions to the trapezoidal sum are accumulated separately. Denoting these contributions by $J(\zeta^+)$ and $J(\zeta^-)$ respectively, we should have

$$J(\zeta^+) + J(\zeta^-) = 0 \tag{3.20}$$

in the limit $\Delta x, \Delta y \to 0$. This check has been applied to every converged solution obtained (§5).

## 4. Experimental arrangement

Experiments have been carried out in the arrangement schematically shown in figure 2. The apparatus consists of two glass disks, which can be driven independently by variable-speed electromotors; the lower disk is fixed to a massive steel ring, supported by roller bearings, which acts as the cylinder sidewall. The diameters of the cylinder and the top disk are respectively 1000 and 960 mm indicating that the width $d$ of the gap between top disk and sidewall is 20 mm. The distance $H$ between the disks can be adjusted continuously in the range 10–100 mm. During the present experiments the distance was fixed at 35 mm, implying that the aspect ratio $\delta$ has a constant value 0·07. The angular speed of the disk can be varied continuously in the ranges 0·1–30 r.p.m. (bottom disk) and 0–60 r.p.m. (top disk). For experiments in the range $200 \leqslant Re^* \leqslant 1000$ the cylinder was filled with ordinary tap water; for smaller $Re^*$ values we used a water/glycerol mixture, thus increasing the kinematic viscosity of the working fluid.

The method of measuring the radial, azimuthal and axial velocity components of the flow is based on the principle of stereophotography, which enables one to determine the position of a point light source (object point) in three-dimensional space. A set of two cameras is used to take simultaneous pictures of the object point $P$ as well as of two fixed reference points ($A$ and $B$), the positions of which are known exactly. The coordinates of the projected object point are measured from both photographs and are related to a common coordinate system defined by the reference points $A$ and $B$, thus yielding the points $P_1$ and $P_2$ (see figure 3). Since the camera view directions are fixed relative to this common reference system, these points $P_1$ and $P_2$ on the lower reference plane correspond to certain points $P'_1$ and $P'_2$ respectively on some upper plane of reference. Once the transformation of an arbitrary point $X$ on the lower plane to its corresponding projection $X'$ on the upper plane of reference is exactly known (for fixed camera positions), the coordinates of $P_1$ and $P_2$ yield the directions $P_1 \to P'_1$ and $P_2 \to P'_2$ respectively. In consequence, the spatial position of the original object point $P$ (being the intersection point of $P_1 P'_1$ and $P_2 P'_2$) is completely determined.

In order to determine fluid velocities, small polystyrene spheres (of diameter 0·3 mm) are added to the fluid, and by dissolving sodium chloride the density of the working fluid is adjusted in such a way that the small particles are neutrally buoyant. Because of their small size the particles move with the surrounding fluid. It is essential that the concentration of tracer particles is low enough to be able to distinguish
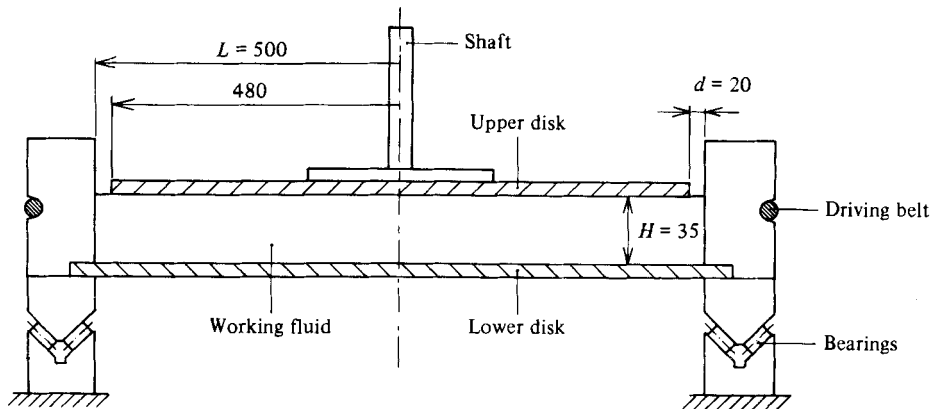
FIGURE 2. The experimental configuration (dimensions in mm).
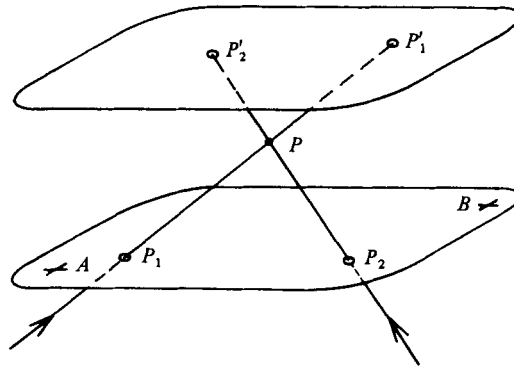


FIGURE 3. Diagram to illustrate the principle of stereophotography.

between the movements of individual particles. The particle motion is visualized by means of a stroboscope producing a number of short light flashes of adjustable frequency. The polystyrene spheres reflect this flash light brightly, and each individual particle acts as a point light source. Each particle path is thus defined by a number of successive 'reflection points' (see figure 4), and by stereophotography the position of these points can be determined accurately. When the flash frequency is known, the distance between two succeeding points on a particular line contains information about the particle velocity along its path. By making the time between the first and second flashes slightly different one is able to discriminate between head and tail of the particle trajectory. In this way we can determine the direction and magnitude of the local fluid velocity. Since the measuring procedure is time-absorbing it has been automated as far as possible. When photographs have been made for a certain flow configuration, an electronic coordinate reader (originally designed for aerial-survey purposes) is used to determine the coordinates of the projected points accurately. These data are put on punch or magnetic tape, from which a computer calculates local velocities for every observed particle path. In this way fluid velocities can be determined within an accuracy of 1 mm/s. This experimental error is sufficiently small for accurate measurement of the azimuthal and radial velocity components. Since the order of magnitude of the axial velocity component is comparable to the experimental error, however, determination of this velocity
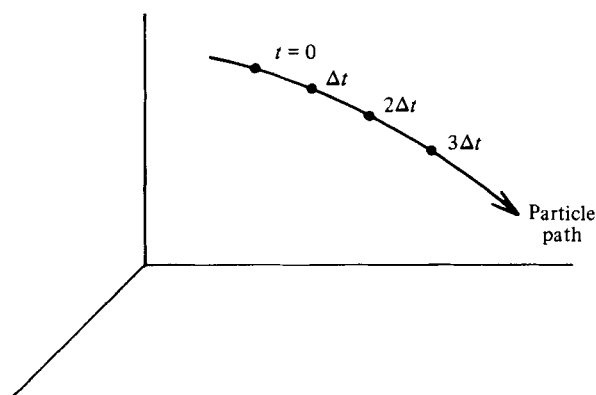
FIGURE 4. By means of a stroboscope each particle path is defined by a number of dots.

component leads to unacceptable relative errors of 100 %, and must therefore be rejected.

In the case of counter-rotating disks ($s < 0$) a stagnation point arises at the slowest rotating disk, as will be discussed below. This stagnation point can easily be visualized by adjusting the fluid density (i.e. the NaCl concentration) in such a way that the tracer particles become slightly buoyant or slightly heavier than the working fluid: for suitably chosen density adjustment, these particles crowd together at the stagnation point, thus producing a clearly observable ring.

## 5. Numerical and experimental results

### 5.1. General remarks

Numerical calculations as well as experiments have been performed for two distinct cases: (i) one disk stationary (§5.2); (ii) disks rotating in opposite senses (§§5.3 and 5.4). For convenience of description we define the inverse rotation ratio $\sigma$ as

$$\sigma = \frac{1}{s} = \frac{\Omega_B}{\Omega_T}. \tag{5.1}$$

When the top disk rotates faster than the bottom disk, i.e. $|s| > 1$, the parameter $\sigma$ will be used.

The behaviour of the numerical procedure is illustrated in table 1, where some global properties of the numerical calculations have been listed. In this table 'central, $21 \times 21$' means central-differencing over a grid with 21 mesh points in both directions (§3). The quantities $J(\zeta^+)$ and $J(\zeta^-)$ denote the positive and negative contribution to the vorticity integral (§3.6); the sum of these two quantities should vanish according to (3.20). Further, $Sw$ gives the number of global alternating direction sweeps required to pass (3.19), whereas 'Time' denotes the seconds CPU time on a Dec-10 computer using Algol-60.

It should be noted that one global sweep involves twice the updating of 3 unknowns at each interior mesh point (§3.4). The grid refinement at $s = -0.3$ shows that the magnitude of the vorticity integral reduces considerably, as it should. However, *more* cycles on the *finer* grid appear to be required, and the resulting CPU time grows in an alarming manner when grid refinement is employed. It is believed that the present *iteration* technique can be improved significantly (e.g. by means of multigrid

| $s$ | $Ek$ | Numerical method | $J(\zeta^+)$ | $-J(\zeta^-)$ | $J(\zeta^+)+J(\zeta^-)$ | $Sw$ | Time (s) |
|---|---|---|---|---|---|---|---|
| 0 | 0·001 | Central, 21 × 21 | 0·057 24 | 0·056 13 | +0·001 11 | — | — |
| −0·3 | 0·01 | Upwind, 21 × 21 | 0·043 56 | 0·043 95 | −0·000 38 | 63 | 180 |
| −0·3 | 0·01 | Upwind, 41 × 41 | 0·044 67 | 0·044 90 | −0·000 23 | 225 | 2800 |
| −0·6 | 0·01 | Upwind, 21 × 21 | 0·042 35 | 0·042 70 | −0·000 35 | 110 | 400 |
| −0·825 | 0·01 | Upwind, 21 × 21 | 0·045 92 | 0·046 24 | −0·000 32 | 215 | 800 |

TABLE 1. Global characteristics of numerical procedure for a few cases

methods). Finally it should be noted that the number of sweeps $Sw$ grows as $s$ decreases towards $-1$. An explanation of this feature will be given in §5.4.

### 5.2. *One disk stationary* ($s = 0$ *and* $\sigma = 0$)

For Ekman numbers $Ek$ in the range 0·001–0·02 both possible cases $\Omega_T = 0$ ($s = 0$) and $\Omega_B = 0$ ($\sigma = 0$) have been investigated experimentally. Numerical calculations have only been performed for the case $s = 0$ and $Ek$ in the range 0·001–1.

Figure 5 shows numerical results for streamfunction $\psi$, vorticity $\zeta$ and azimuthal velocity $v$ at $Ek = 0·01$ ($s = 0$), while corresponding graphs at $Ek = 0·001$ are presented in figure 6. Qualitatively the results are in agreement with the ones calculated by Lugt & Haussling (1973) taking the differences in aspect ratios into account.

It should be noted that throughout this paper the value of the cylinder aspect ratio is $\delta = 0·07$ for experiments as well as numerical work, but for graphical resolution the axial scale in the figures has been blown up. It turns out that variation of $Ek$ from 0·01 to 0·001 does not affect the flow character dramatically. The major modification takes place in the disk boundary layers, which thicken with increasing Ekman number. At $Ek = 0·001$ viscous effects are mainly confined to the disk boundary layers and a layer at the cylinder sidewall. The smallness of the disk boundary-layer thickness ($\approx (Ek)^{\frac{1}{2}}$) imposes severe demands on the grid used in the numerical work: a numerical exercise at $Ek = 0·001$ with a *uniform* axial grid revealed the presence of grid oscillations in the converged solution; the oscillations disappeared completely when the transformation in axial direction was activated (§3.2). The effect of the transformation is illustrated in the appendix (figure 16).

The main character of the flow at $s = 0$ will now be outlined. Owing to the centrifugal action of the rotating disk, fluid flows from the top to the bottom disk. The disk boundary layers carry the fluid radially outwards over the bottom disk and inward along the stationary upper disk. In the shear layer at the sidewall fluid moves upward. Figure 6(c) reveals that a substantial part of the fluid outside the disk boundary layers is rotating in agreement with Batchelor's (1951) predictions for infinite disks.

Figure 7 shows some characteristic tangential-velocity profiles at $Ek = 0·001$; experimental data are depicted by dots. Because the tracer particles used in the experimental work are randomly distributed in the working fluid, it is unlikely that several particles are present on a given radius when a photograph is taken. Therefore the experimental data are arranged in small radius intervals $\Delta r = r_{\max} - r_{\min}$. In order to compare with experimental data, the numerical results are drawn for values as close as available near $r_{\min}$ and $r_{\max}$. It may be seen from figure 7 that the experimental values of the tangential velocity are in perfect agreement with the
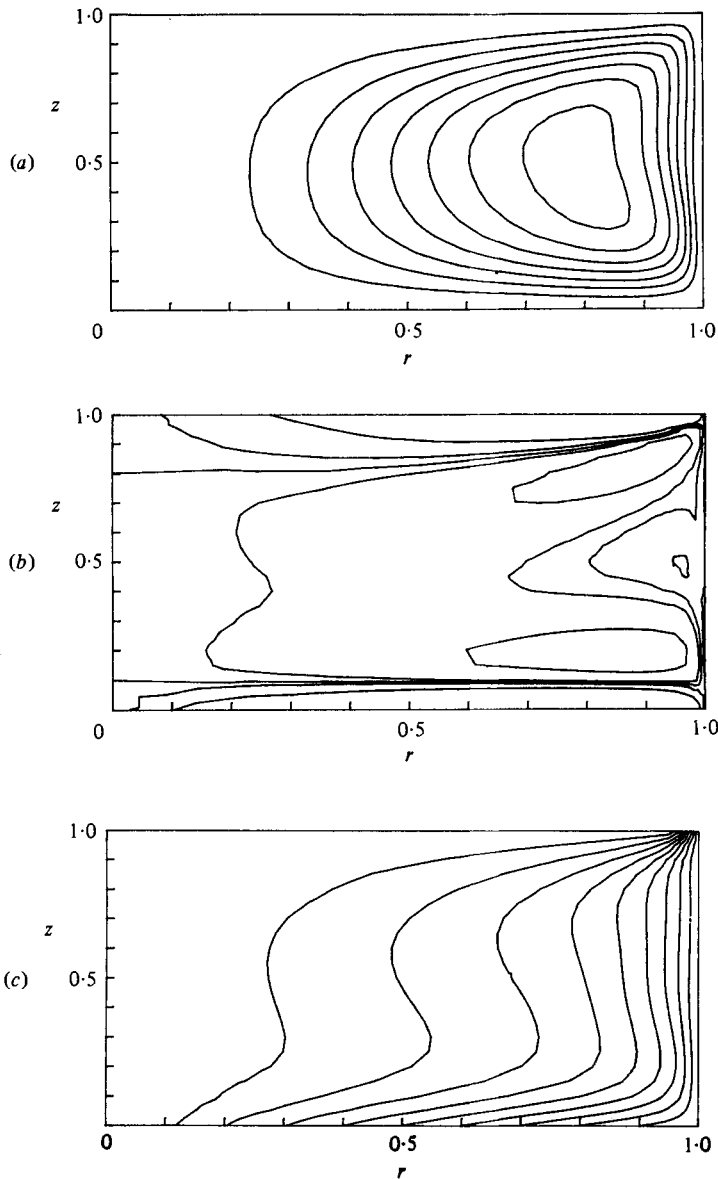
FIGURE 5. Numerical results for $s = 0$, $Ek = 0.01$: (a) streamlines $10^4 \psi = 25(25)175$; (b) lines of constant vorticity; (c) lines of constant azimuthal velocity $v = 0.1(0.1)0.9$.

numerical data; good agreement is also found in the radial-velocity component (not displayed). The axial velocity resulting from the numerical calculations cannot be compared with experimental data since the latter are not available: the error in the experimental values is of the same order as the magnitude of the axial velocity component. Further information on the axial velocity may be found in the appendix.

The influence of the sidewall is illustrated in figure 8, where the azimuthal velocity $v$ in the bulk (i.e. outside disk-boundary layers) is displayed for the cases $s = 0$ and $\sigma = 0$ (at $Ek = 0.001$). In the central core of the flow region, the swirl velocity is seen to be a linear function of the radius $r$: $v = 0.33r$ for the range $0 \leqslant r \leqslant 0.5$ (at $s = 0$). This is in agreement with von Kármán's similarity hypothesis for infinite disks; in
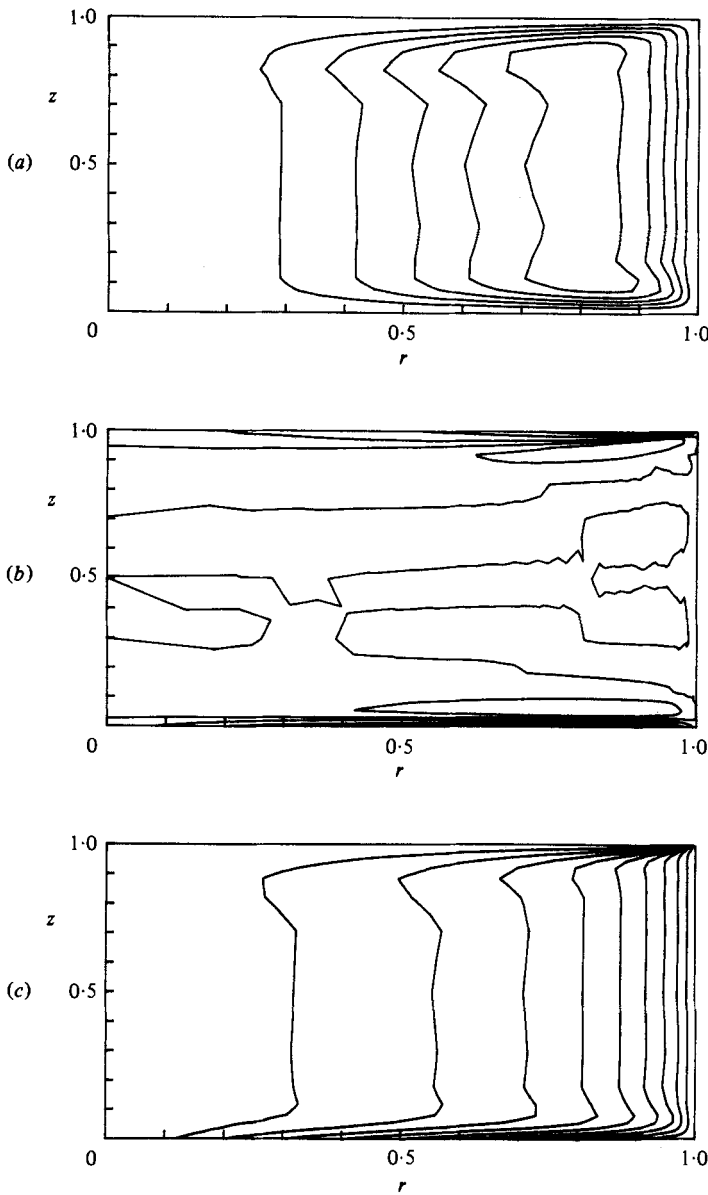
FIGURE 6. Numerical results for $s = 0$, $Ek = 0.001$ (sharp corners are due to the mesh-point distribution): (a) streamlines $10^4 \psi = 10(10)50$; (b) lines of constant vorticity; (c) lines of constant azimuthal velocity $v = 0.1(0.1)0.9$.

the limit $Ek \to 0$ this hypothesis yields for the Batchelor solution: $v = 0.313r$ at $s = 0$, outside boundary layers (see also the appendix).

Owing to the presence of the cylinder sidewall this linear behaviour with $r$ cannot persist up to $r = 1$, where the boundary condition on $v$ dictates that $v = 1$ for $s = 0$, and $v = 0$ for $\sigma = 0$. In the latter case where the bottom disk and the sidewall are stationary, only experimental data are available and it may be seen from figure 8 that the linear behaviour of the swirl velocity holds over a larger range ($0 \leqslant r \leqslant 0.75$) than in the case $s = 0$. Obviously this effect is caused by the non-rotating sidewall.
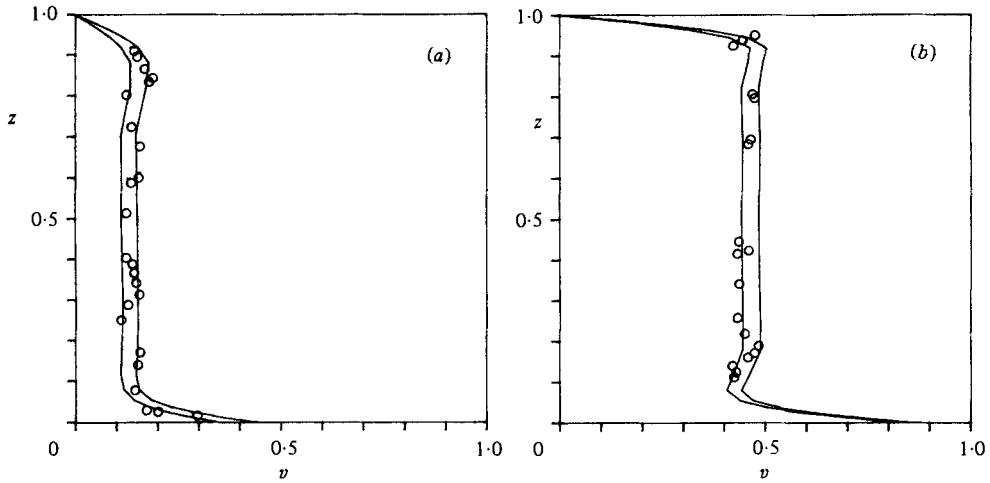
FIGURE 7. Comparison between results for the tangential velocity at $s = 0$, $Ek = 0.001$: ———, numerical results; $\bigcirc$, experimental values. (a) $r_{min} = 0.36$, $r_{max} = 0.45$; (b) $r_{min} = 0.84$, $r_{max} = 0.87$.
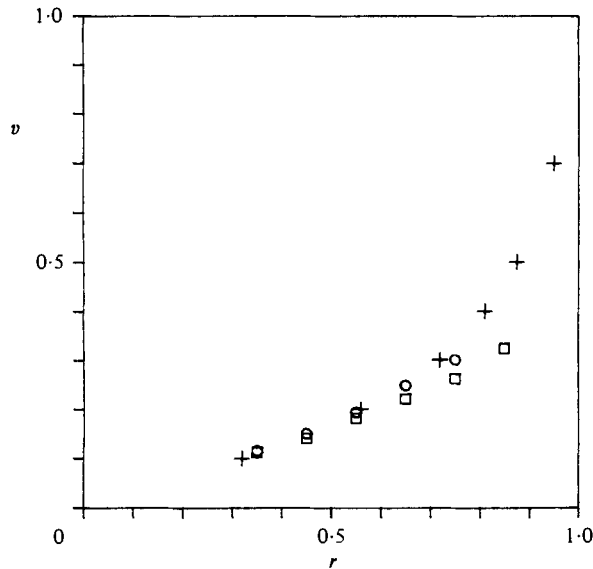


FIGURE 8. The swirl velocity $v(r,z)$ at the midplane $z = 0.5$ for the case $s = 0$, $Ek = 0.001$: $+$, numerical data; $\bigcirc$, experimental values. $\square$, experimental values at $\sigma = 0$, $Ek = 0.001$. Note the linear behaviour at moderate radii.

## 5.3. *Disks rotating in opposite senses*

For counter-rotating disks numerical results have been obtained at $Ek = 0.01$ for several values of $s$ in the range $0 > s \geqslant -0.825$. The numerical method for these cases uses upwind differencing with $21 \times 21$ grid points. At $s = -0.3$ grid refinement revealed that the error in the solution on the coarse grid was of the order of $10\%$ or less. A comparison between the results for the two grids may be found in the appendix (figure 17).

The flow structure will now be considered for two selected values of $s$, viz $s = -0.3$ and $s = -0.825$.
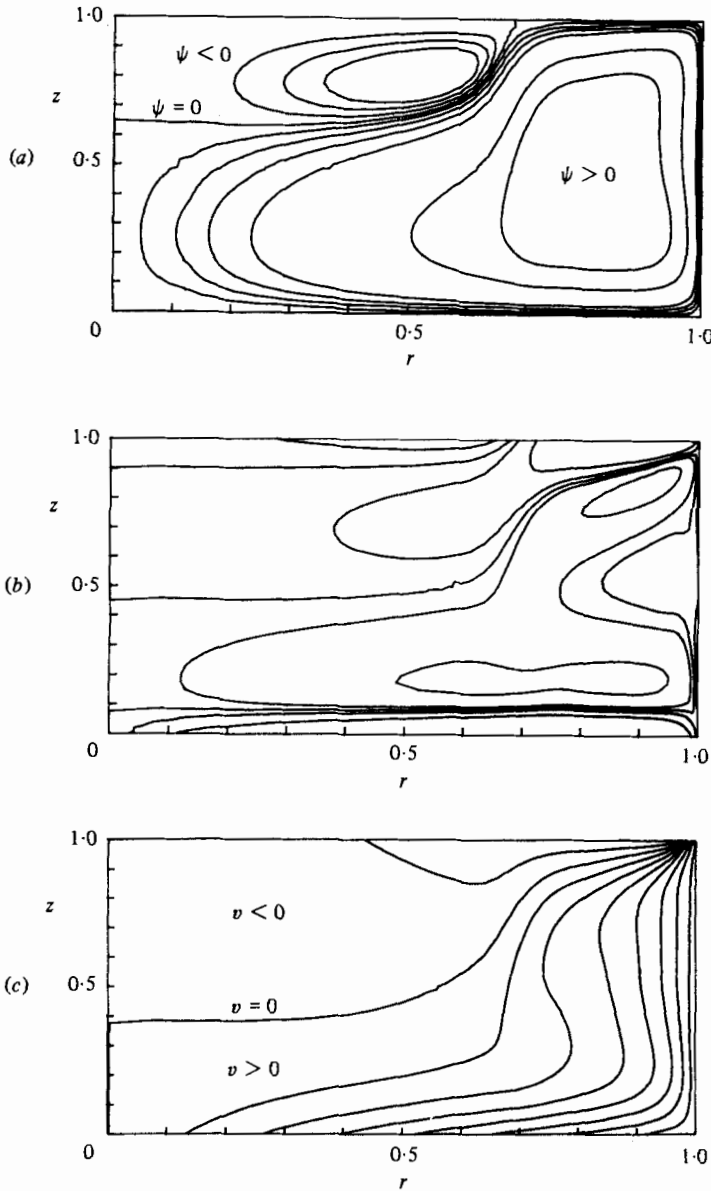
FIGURE 9. Numerical results for $s = -0.3$, $Ek = 0.01$: (a) streamlines $10^4 \psi = -3(1)1$, $2.5$, $5$, $10$, $50$, $100$; (b) lines of constant vorticity; (c) lines of constant azimuthal velocity $v = -0.1(0.1)0.7$.

5.3.1. *The case $s = -0.3$ ($Ek = 0.01$)*. Figure 9 shows numerical results for $\psi$, $\zeta$ and $v$, and it reveals a remarkable feature of the flow at negative $s$-values: the flow in the meridional plane has a two-cell structure. The dividing stramline $\psi = 0$ ends at the upper (slower-rotating) disk, thus forming a stagnation point in the meridional plane at $r_{st} = 0.67$. In the experimental arrangement this point corresponds to a stagnation ring at the upper disk.

The two-cell structure may be explained on the basis that the faster-rotating disk dominates the flow behaviour: the outward radial flow over the bottom disk induces a downward axial interior flow. At the sidewall a thin layer carries fluid vertically
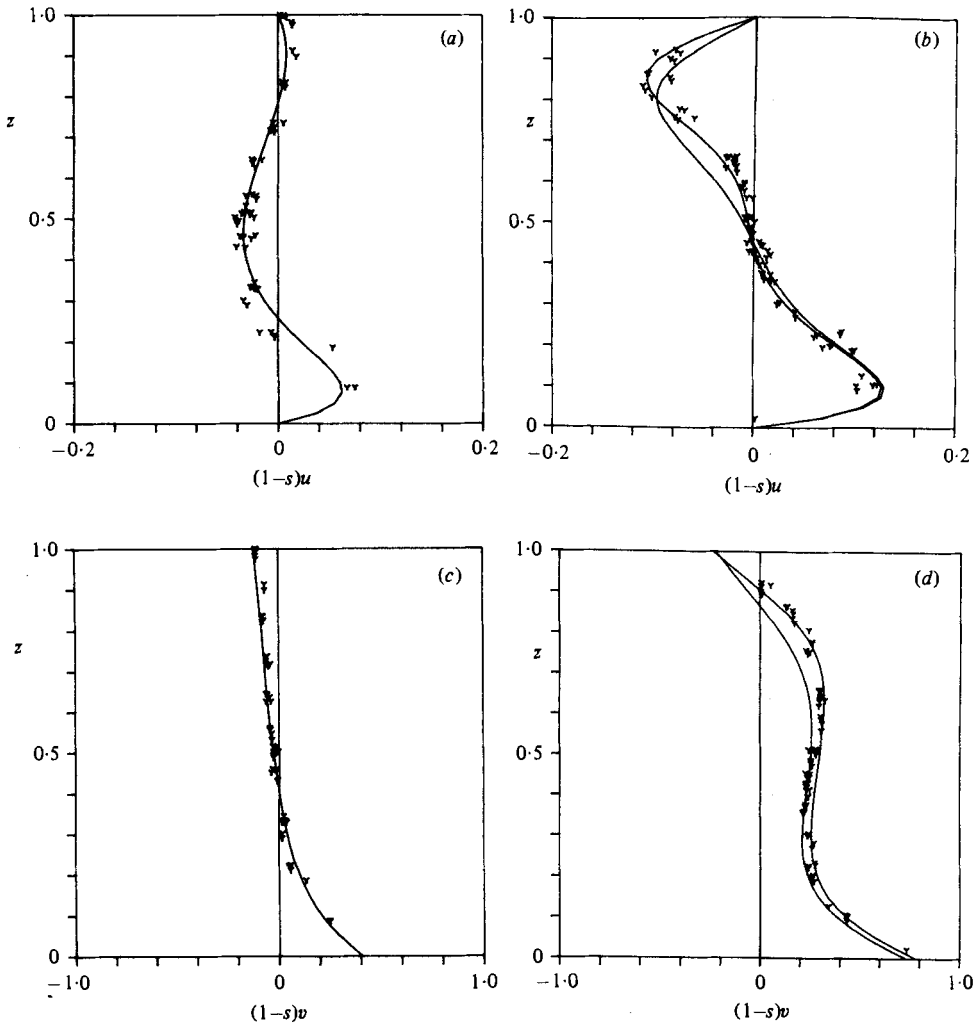
FIGURE 10. Comparison between results for the radial $(a, b)$ and the azimuthal $(c, d)$ velocities at $s = -0.3$, $Ek = 0.01$: ———, numerical results; $\gamma$, experimental values. $(a, c)$ $r_{min} = r_{max} = 0.41$; $(b, d)$ $r_{min} = 0.74$, $r_{max} = 0.78$.

upwards, which results in an inward radial flow along the slower-rotating upper disk. Near the axis of rotation, however, the upper disk produces an outward radial flow which meets the inward radial flow at the stagnation point, where the fluid must flow downwards along the dividing streamline $\psi = 0$ (figure 9a). Figure 9(c) shows that the upper and lower parts of the fluid rotate in the same sense as the upper and lower disks respectively. It is worth noting that the dividing line $v = 0$ between the 'swirl-velocity cells' does not coincide with the dividing streamline $\psi = 0$ for this value of $s$.

Numerical and experimental profiles of the tangential and radial velocity are presented in figure 10 at two selected values of the radius. Again it is seen that there is good agreement between experimental data and numerical results. At small or moderate values of the radius, as figure 10(c) reveals, the swirl velocity changes continuously from the lower to the upper disk, reversing approximately at the midplane; however, at larger radii (figure 10d) a substantial part of the fluid rotates
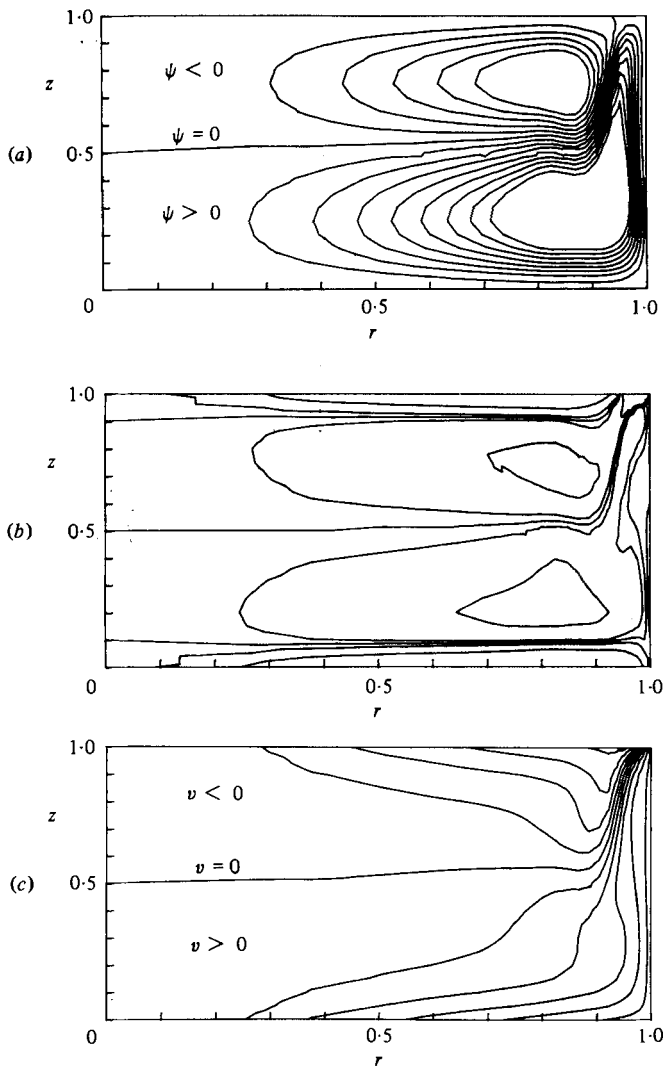
FIGURE 11. Numerical results for $s = -0.825$, $Ek = 0.01$: (a) streamlines $10^4 \psi = -50(10)80$; (b) lines of constant vorticity; (c) lines of constant azimuthal velocity $v = -0.4$, $-0.3$, $-0.2$, $-0.125$, $0$, $0.15$, $0.2(0.1)0.5$.

in the same sense as the bottom disk, indicating a Batchelor type of flow sufficiently far from the axis of rotation. The nature of the flow at smaller radii seems to be of Stewartson type (virtually no rotation outside the disk boundary layers). For further comment with regard to this feature see §5.4 and the appendix.

It may be seen from figure 10 that the tracer particles were apparently slightly lighter than the working fluid, so that only a few particles were left in the bottom-disk boundary layer.

5.3.2. *The case* $s = -0.825$ *(Ek = 0.01).* Numerical results for $s = -0.825$ are shown in figure 11, and it is clear that the influence of the top disk has grown significantly as compared with the case $s = -0.3$. The stagnation point is now at $r_{st} = 0.94$, and it follows that its location depends strongly on $s$. Note that the gap (figure 2) between top disk and cylinder sidewall occupies the range $z = 1$,

$0.96 < r < 1$, so that the stagnation point has almost entered the gap. It is probably for this reason that no reliable results (either numerical or experimental) have been obtained in the range $-1 \leqslant s < -0.825$. The numerical procedure failed to converge in this range, and at the same time wavelike instabilities appearing in the experimental arrangement near the sidewall prevented further accurate measurements. In addition it should be remarked that no observations could be made of the flow near the gap $z = 1$, $0.96 < r < 1$. This was caused by the presence of a steel ring supporting the bottom disk. Measurements could only be performed up to about 3 cm from the sidewall.

From figure 11 $(a, c)$ the lines $\psi = 0$ and $v = 0$ appear to be coincident, except near $r = z = 1$. Note also the symmetry about the midplane over the range $0 \leqslant r \leqslant 0.8$. Although even at $s = -1$ the flow pattern cannot be exactly symmetrical about the midplane (since the sidewall is fixed to the bottom disk) it is clear that there is a strong tendency to this symmetry over the major part of the region occupied by the fluid. This property is further illustrated in figure 12, where numerical results for radial and tangential velocities are shown. Experimental data for the values of the parameters considered are not available, so that no comparison can be made.

At small radii the tangential velocity (figure 12$c$) changes continuously from lower to upper disk, similar to the case $s = -0.3$; however, the swirl velocity profile at larger radii (figure 12$d$) seems to indicate the presence of a *transition* layer at the midplane. The cells on both sides of this layer rotate with equal but opposite angular velocities. This type of flow has been predicted by Batchelor (1951), but it should be remarked that profiles with a transition layer are encountered in the present work at radius values where the similarity hypothesis does not hold.

### 5.4. *Stagnation point*

The main characteristic feature of the flow for the case of counter-rotating disks $(s < -0.1)$ enclosed by a cylinder is the appearance of one single stagnation point at the slower-rotating disk. Associated with the stagnation point there is a two-cell structure in the meridional plane as shown in §5.3.

For a confined configuration a two-cell structure has been reported by Lugt & Haussling (1973). They calculated numerical solutions at an aspect ratio $\delta = 1$ and obtained a two-cell structure at $Ek = 0.01$ for some values of $s$ down to $-9$. For $s < -9$ $(\sigma > -0.11)$ the flow had achieved a single-cell pattern again. These results are in agreement with the present investigation as will be shown below.

For several values of $s$ in the range $-0.1 > s > -0.825$ and $Ek = 0.01$, the location $r_{st}$ of the stagnation point has been calculated. Experimental evidence is obtained by adding small buoyant particles to the working fluid in order to visualize the formation of a stagnation ring at the slower-rotating upper disk $(s > -1)$. Because of their smaller density the particles are pressed against the top disk, where radial forces cause them to move towards the stagnation point (see figures 9 and 11). In the stationary situation the particles thus form a ring at the top disk and move with this disk in the tangential direction (see figure 13). By means of particles of larger density, the stagnation ring at the bottom disk $(s < -1)$ can be visualized similarly.

Although the thickness of the ring increases as $|s|$ becomes smaller, the radius $r_{st}$ of the particle ring can be measured accurately. Experimentally, the location of the ring is found to possess a high degree of reproducibility independent of the starting conditions. From the experiments it also appears that the formation time for the particle ring to settle down, strongly increases as $r_{st} \to 0$: at $Ek = 0.01$ the formation

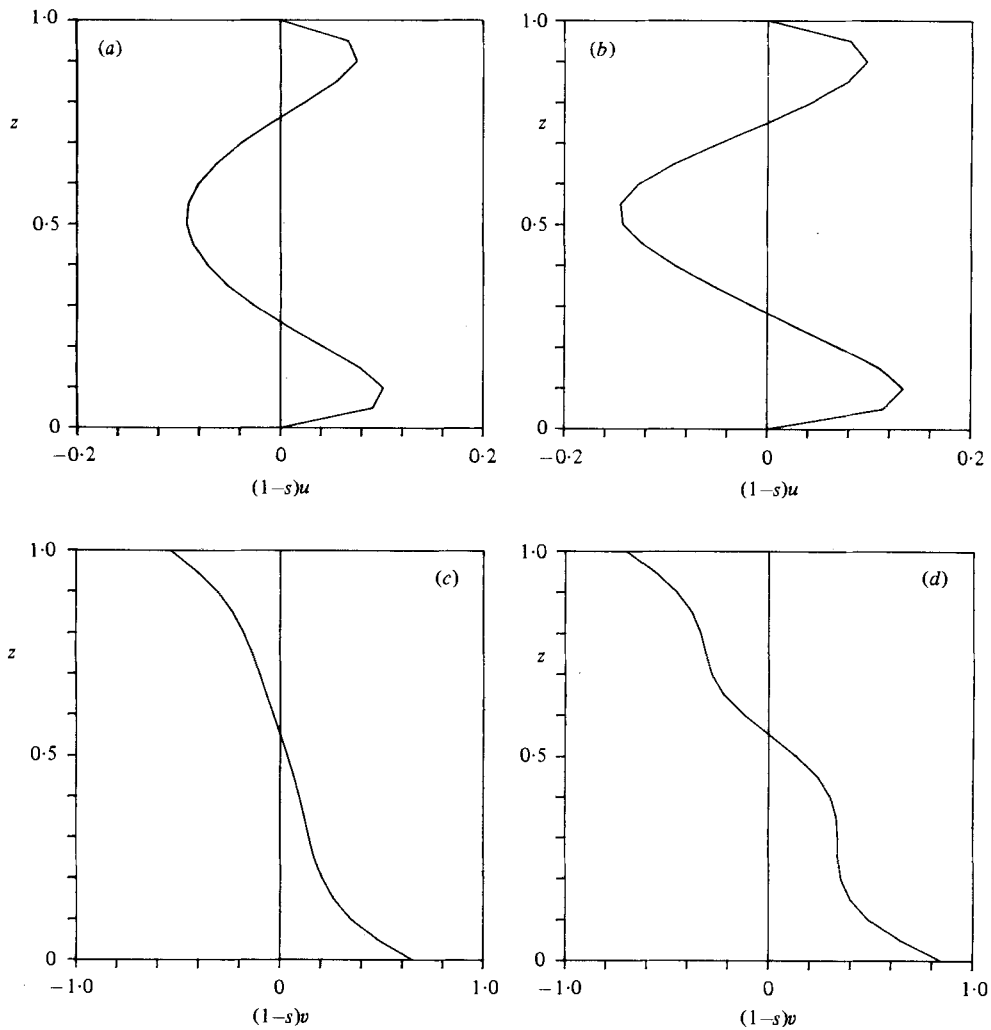FIGURE 12. Numerical results for the radial $(a, b)$ and the azimuthal $(c, d)$
velocities at $s = -0.825$, $Ek = 0.01$: $(a, c)$ $r = 0.652$; $(b, d)$ $r = 0.848$.

time is about 5 min for $r_{st} = 0.9$ $(s = -0.7)$, but approximately 2 h for $r_{st} = 0.2$ $(s = -0.15)$.

Experimental and numerical results for the case $Ek = 0.01$ are shown in figure 14, and it is clear that there is satisfactory agreement.

Despite the presence of a free surface (or gap) at $z = 1$, $0.96 < r < 1$, figure 14 reveals that $r_{st} \to 1$ as $s \to -1$. However, experiments at $s = -1$ revealed an unstable flow near the sidewall (wavelike instabilities over the free surface) so that no particle ring could be observed.

Experiments in the range $s < -1$ $(-1 < \sigma < 0)$ showed a behaviour of the stagnation ring similar to the case $s > -1$, but now at the bottom disk: starting from $\sigma \approx -0.15$ to $\sigma = -1$ the radius $r_{st}$ increases, as may be seen from figure 14.

In the range $-0.1 < s$, $\sigma < 0$ no particle ring has been observed, not even several hours after starting the flow. Apparently, the relative amount of counter-rotation, measured by $|s|$ or $|\sigma|$, must exceed a certain value in order that a stagnation point
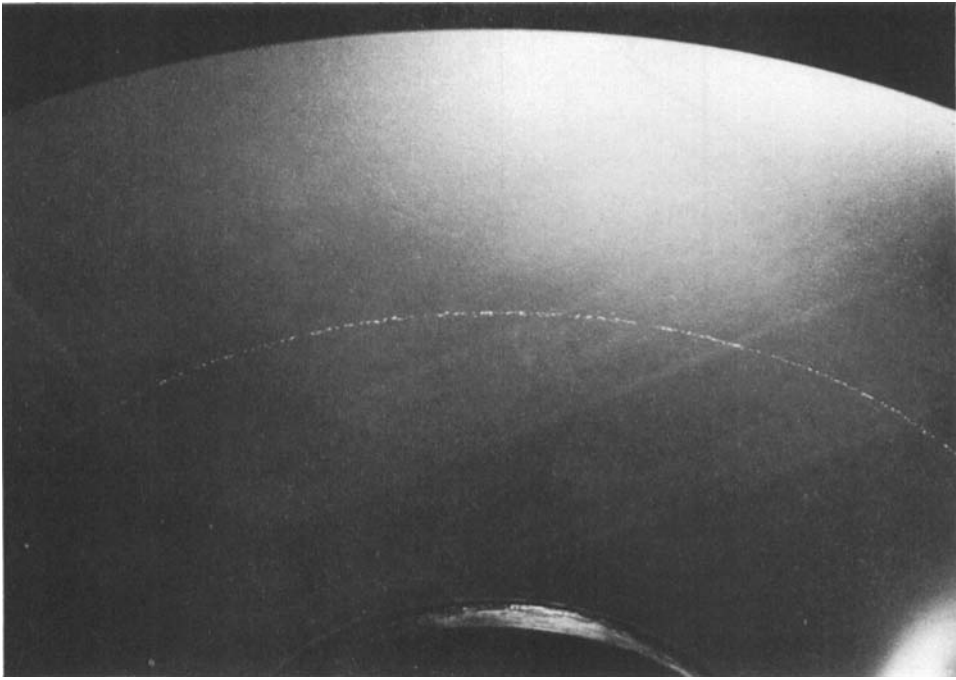
FIGURE 13. An example of the stagnation ring appearing in the experimental configuration.
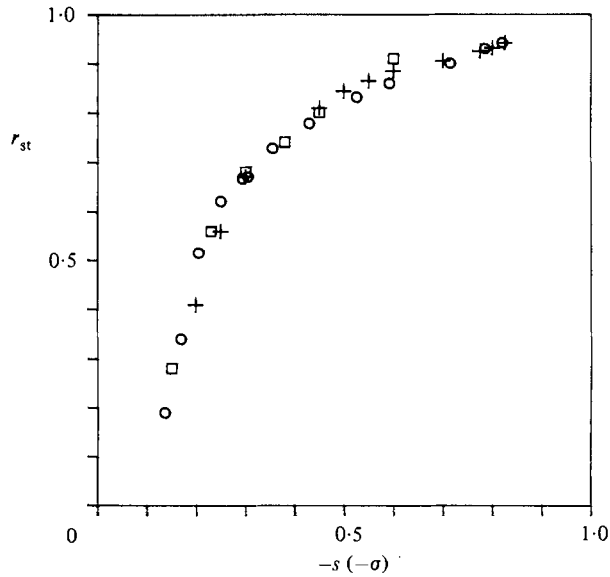


FIGURE 14. The location $r_{st}$ of the stagnation point for various rotation ratios at $Ek = 0.01$: $+$, numerical values at top disk $(-1 < s < 0)$; $\bigcirc$, experimental data at top disk $(-1 < s < 0)$; $\square$, experimental data at bottom disk $(-1 < \sigma < 0)$.

may appear. This is also in agreement with the results reported by Lugt & Haussling (1973). For more details on this feature see the appendix.

Additional experiments have been performed for $Ek \neq 0.01$, and the results are shown in figure 15, where $r_{st}$ has been plotted versus $\log Re^* = -\log Ek$ for several values of $s$. In the range $-0.7 < s < -0.4$ the position $r_{st}$ of the stagnation point is
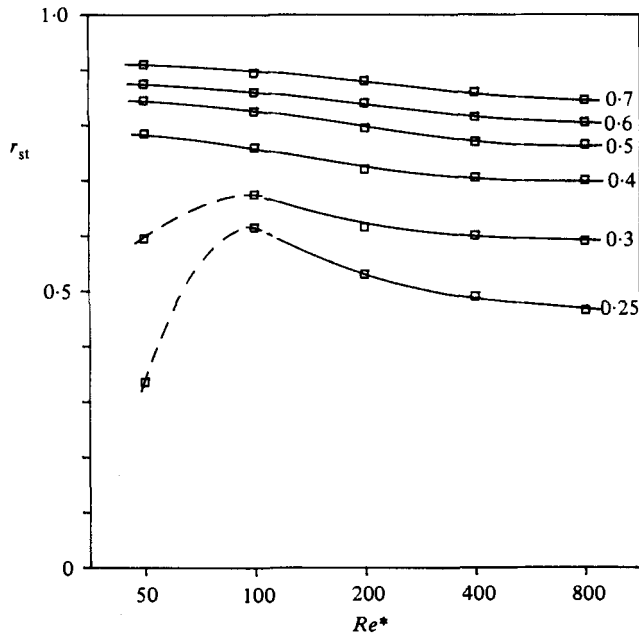
FIGURE 15. The position of the stagnation point $r_{st}$ versus Reynolds number $Re^* = 1/Ek$. Experimental values in the range $-1 < s < 0$. Parameter on curves is $|s|$.

seen to decrease with increasing $Re^*$, but at smaller values of $|s|$ a maximum appears near $Re^* \approx 100$. This means that (for the lower $|s|$ values), starting from $Re^* = 50$ the stagnation ring shifts radially outward until a maximum is reached at $Re^* \approx 100$; increasing $Re^*$ beyond 100 causes the ring to shrink again towards a final position at large $Re^*$.

The present laboratory arrangement did not permit reliable experiments for $Re^* < 50$, because of small instabilities in the driving mechanism, but future work, supported by numerical calculations, could possibly reveal some interesting features of the flow in this regime.

It is worth making a final comment on the additional experiments described above. At $s = -0.6$, $Re^* = 1000$ and $s = -0.45$, $Re^* = 500$ experiments have revealed the presence of Stewartson profiles over a significant range $0 < r < 0.6$: in this range the azimuthal velocity virtually vanishes outside the disk boundary layers. However at $s = -0.15$, $Re^* = 500$ a definite bulk rotation was observed, indicating the presence of a Batchelor profile. In §5.2 we have shown that at $s = 0$, $Re^* = 1000$ the flow near the axis of rotation is also of Batchelor type and it follows that for the present confined geometry either Stewartson or Batchelor profiles are relevant at large values of $Re^*$ in a neighbourhood of the axis of rotation. Which profile actually appears strongly depends on $s$ and therefore on the location of the stagnation point.

## 6. Conclusions

When the top disk is stationary ($s = 0$), calculations and experiments show that a substantial part of the fluid outside the disk boundary layers is in solid-body rotation, in agreement with Batchelor's (1951) predictions for the flow between infinite disks.

When the disks rotate in opposite senses with $s < -0.15$, the flow in the meridional

plane appears to have a two-cell structure similar to that calculated by Lugt & Haussling (1973). The dividing streamline $\psi = 0$ between both cells ends at the slower-rotating disk, thus forming a stagnation point. In physical reality this point corresponds to a stagnation ring at the slower-rotating disk; its existence has been demonstrated both numerically and experimentally. The location of the ring depends on the parameters $s$ and $Re^*$. It has been computed for several values of $s$, and the results are in good agreement with experimental observations. Experimentally the stagnation point possesses a high degree of reproducibility, independent of the starting conditions. In the range $-0.15 < s \leqslant 0$ no stagnation ring has been observed, and a mathematical argument for this feature (on the basis of similarity equations) has been put forward.

As $s$ decreases towards $-1$, the computed flow pattern away from the cylinder sidewall tends to a symmetrical two-cell structure: upper and lower cells rotate in the same sense as the adjacent disk, and at the midplane the swirl velocity changes sign. Although the Reynolds number is not very large ($Re^* = 1/Ek = 100$), the numerical results seem to indicate the existence of a viscous transition layer between both cells, sufficiently far away from the axis of rotation. Profiles with a transition layer have been predicted by Batchelor (1951), but at the radii where transition layers are encountered in the present investigation the similarity demands are not satisfied. Near the axis of rotation, however, the similarity transformation is valid indeed, and the solution is more in agreement with a Stewartson profile provided that the counter-rotation is sufficiently strong: later experiments at $Re^* = 1000$ and $s = -0.6$ have revealed that in the range $0 < r < 0.6$ the angular velocity virtually vanishes outside the disk boundary layers.

On the basis of material presented in this paper, we conclude that (depending mainly on $s$) either Batchelor or Stewartson profiles are adequate for the description of a part of the flow in a confined configuration such as the present one. In addition we conclude that for arrangements with a *sidewall* all higher-branch similarity solutions as calculated by numerous authors are unlikely to occur in physical reality: the cylinder sidewall eliminates all higher branch possibilities.

## Appendix. Similarity considerations

The purpose of this appendix is to present a comparison of the results obtained for the confined geometry with data calculated on the basis of the similarity equations.

It is found that the region where the von Kármán similarity equations govern the flow depends strongly on the position of the stagnation point. At $s = 0$, $Ek = 0.001$ there is no stagnation point and over 50 % of the radius the flow is of similarity nature (Batchelor type). At $s \approx -0.15$ a stagnation point appears near $r = 0$ at the top disk, and the region where the similarity equations hold is very small, while it grows again if the stagnation point moves outward, i.e. $s \to -1$. In this case the relevant similarity solution is of Stewartson type for $Ek$ small enough. In addition it is found that – in

general – the agreement between the similarity data and the results for the confined cylinder is better near the faster-rotating bottom disk than near the slower-rotating top disk ($-1 < s < 0$). This may be explained by the intuitively clear assumption that the faster-rotating disk dominates the flow (§5.3). Hence the flow near the slower-rotating disk is much more affected by the presence of the radial boundary. Along the sidewall, fluid moves towards the slower-rotating disk and subsequently inward over that disk (or part thereof). From papers by Nguyen *et al.* (1975) and Holodniok *et al.* (1977, 1981) it is known that the similarity equations for the two-disk problem have non-unique solutions if the Reynolds number is large enough. At $Re^* = 625$ for instance, Holodniok *et al.* (1981) calculated a multiplicity of similarity solutions for several values of $s$. However, it will be shown in §§A 2 and A 3 that of this multiplicity of solutions only two branches are relevant to the present confined problem. In terms of the nomenclature developed by Holodniok *et al.* these branches are branch 1 (Batchelor-type) and branch 8 (Stewartson-type).

Therefore we believe that the original papers by Batchelor (1951) and Stewartson (1953) are still of fundamental relevance to rotating flows in confined containers.

### A.1. *Similarity equations and method of solution*

Since numerical results for the confined geometry have been calculated in the range $-1 < s \leqslant 0$, we will consider only this range of $s$-values so that $\Omega_B > |\Omega_T|$. The parameters appearing in (2.1)–(2.9) are then given by

$$s = \frac{\Omega_T}{\Omega_B}, \quad Ro = 1-s, \quad Ek = \frac{\nu}{H^2\Omega_B}, \quad Re^* = \frac{1}{Ek}, \quad a = \frac{1}{Ro} = \frac{1}{1-s}. \quad \text{(A 1)}$$

In terms of the stream function $\psi$ and the tangential velocity $v$ the von Kármán similarity hypothesis may be written in the form

$$\psi = r^2 f(z), \quad v = rg(z). \quad \text{(A 2)}$$

The remaining quantities of interest then follow from (2.10), viz

$$u = rf'(z), \quad w = -2f(z), \quad \zeta = rf''(z). \quad \text{(A 3)}$$

Substitution into the governing equations (2.11)–(2.13) produces the following ordinary differential equations:

$$\left. \begin{array}{l} \epsilon^2 f^{iv} + 2ff''' + 2gg' = 0, \\ \epsilon^2 g'' + 2fg' - 2f'g = 0 \end{array} \right\} \quad \text{(A 4)}$$

($\epsilon^2 = Ek/Ro$, $' \equiv d/dz$), with boundary conditions at the disks from (2.14):

$$\left. \begin{array}{l} f(0) = f'(0) = f(1) = f'(1) = 0, \\ g(0) = a = \dfrac{1}{1-s}, \quad g(1) = sa = \dfrac{s}{1-s}. \end{array} \right\} \quad \text{(A 5)}$$

The proposed structure (A 2), (A 3) satisfies the boundary conditions along the axis $r = 0$, but the conditions (2.14) at the sidewall $r = 1$ are violated so that the similarity solution will deviate from the true solution of the confined problem in a certain neighbourhood of $r = 1$. In fact the region of validity of similarity assumptions may be better described in terms of the stagnation point (see the introductory lines of this appendix).

We now consider the numerical method that has been used to solve the equations

(A 4). Note that the equation for $f$ may be integrated once, whence (A 4) becomes:

$$\left.\begin{array}{l} \epsilon^2 f''' + 2ff'' - f'^2 + g^2 = C, \\ \epsilon^2 g'' + 2fg' - 2f'g = 0, \end{array}\right\} \tag{A 6}$$

where $C$ is a constant independent of $z$.

The equations (A 6) with boundary conditions (A 5) have been solved with a finite-difference method and Newton iteration to cope with nonlinearity. In fact the finite-difference procedure developed by Zandbergen & Dijkstra (1977) for solving *single-disk* problems appeared to be suitable for the present two-disk problem as well. The only modifications consisted of a rescaling and an additional iteration loop on the constant $C$ in (A 6). For a single-disk problem $C$ is *a priori* known, but for a two-disk problem it has to be determined along with the solution. For further details concerning the finite-difference technique and the Newton iteration see Zandbergen & Dijkstra (1977).

### A.2. *Comparison between results for the confined configuration and results based on similarity considerations*

In this subsection we compare the numerical results obtained from the similarity equations (A 5) and (A 6) with the results calculated for the confined geometry described elsewhere in this paper. For the sake of brevity we restrict ourselves to the values of $s$ selected in §§5.2 and 5.3, viz $s = 0$, $-0.3$ and $-0.8$.

A.2.1. *The case $s = 0$* (figure 16). For a stationary top disk and $Ek = 0.001$ $(Re^* = 1000)$ axial distributions of the tangential and radial velocities are presented in figure 16(a), while figure 16(b) shows the axial velocity and the vorticity. The value of $r$ at which the results are depicted is $r = 0.2233$, which is the first grid line $r = \mathrm{constant}$ to appear near the axis $r = 0$ in the confined calculations with $21 \times 21$ mesh points (§3.3). The confined results have been obtained with central differences, and half of the axial mesh points are presented in the figures. Note the non-uniform distribution of these axial mesh points, which shows the effect of the transformation (3.2). The full lines are the profiles obtained with the similarity equations. In order to be sure that the similarity results are sufficiently accurate much more mesh points have been used as compared with the axial grid for the confined solution.

From the behaviour of the profiles and the perfect agreement between the results of the two calculations the following conclusions can be drawn.

(i) The transformation (3.2) has the desired effect, namely to furnish mesh points where they are required.

(ii) The von Kármán similarity hypothesis predicts a flow which is in perfect agreement near the axis of rotation with the real flow in a confined container.

(iii) At $s = 0$ and large $Re^*$, all quantities displayed in figure 16 are constant outside the two disk boundary layers.

It will be clear from figure 16 that the flow in the case $s = 0$ is of Batchelor type. In his paper Batchelor (1951) has put forward an interesting argument on the basis of which the velocities in the bulk can be calculated from two basic *single*-disk similarity solutions. The value of the tangential velocity in the bulk should be such that the axial velocities predicted by the two associated single-disk boundary-layer similarity solutions are the same. The present authors were in the possession of these latter solutions so that we could carry out this match. We obtained in the bulk region between the disks

$$\frac{\Omega}{\Omega_{\mathrm{B}}} = 0.313, \quad \frac{w}{\epsilon} = -0.755 \quad \mathrm{as} \quad \epsilon \to 0 \quad (s = 0),$$
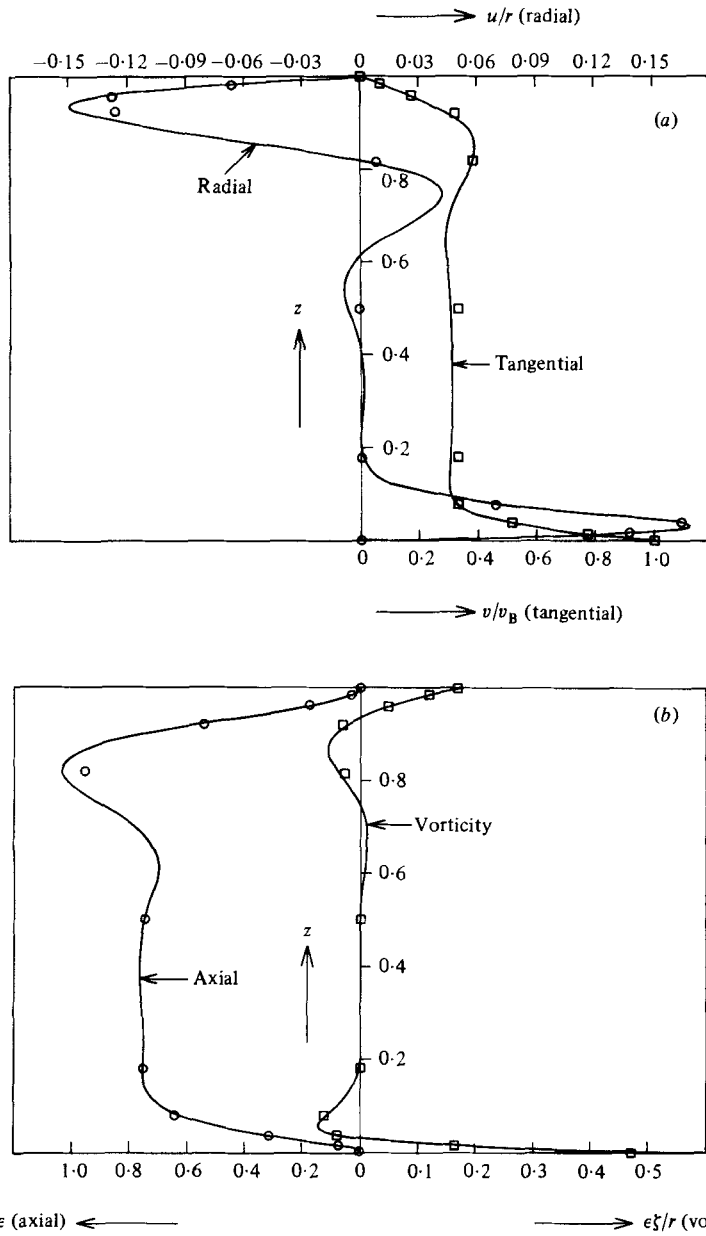
FIGURE 16. Comparison between numerical results at $r = 0.2233$, $s = 0$, $Ek = 0.001$; $\epsilon = Ek^{\frac{1}{2}}$, $v_B = v$ at bottom disk: ——, similarity solution; □, ○, full partial differential equations, grid $21 \times 21$ (half of axial mesh points shown). (a) radial and tangential velocities; (b) axial velocity and vorticity. Note the non-uniform distribution of axial grid points.

where $\Omega_B$ denotes the angular velocity of the bottom disk and $\epsilon = 1/Re^{*\frac{1}{2}} = Ek^{\frac{1}{2}}$. These results are in perfect agreement with the values presented in figure 16.

A.2.2. *The case* $s = -0.3$ *(figure 17)*. For values of $s < 0$, the calculation of the confined solution as described in §3.3 uses upwind differencing. Consequently, the error may turn out to be larger than in the central mode used at $s = 0$.

The case $s = -0.3$ is of particular interest, since in this case numerical solutions
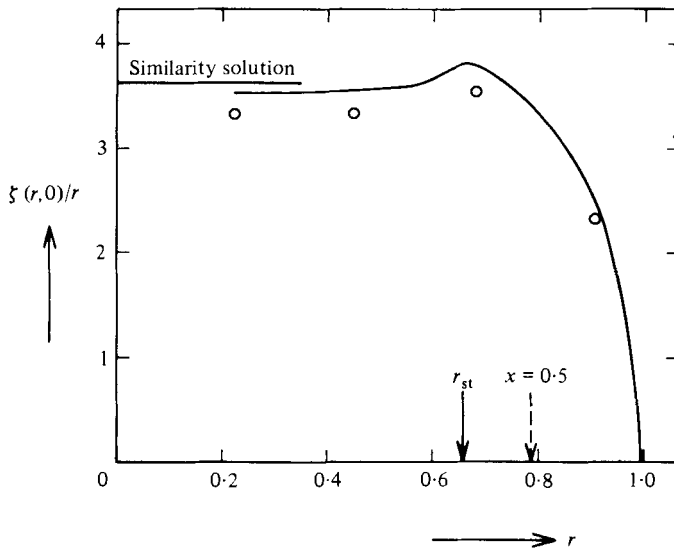
FIGURE 17. Bottom-disk vorticity divided by $r$ for $s = -0.3$, $Ek = 0.01$: ———, grid $41 \times 41$; $\bigcirc$, grid $21 \times 21$. $r_{st} = r$-coordinate of stagnation point at top disk. Note the position of the computational coordinate $x = 0.5$.

have been computed with two grids, namely $21 \times 21$ and $41 \times 41$. We select the radial distribution of the bottom-disk vorticity for the present comparison (figure 17). According to similarity principles, (A 3), the vorticity when divided by $r$ should be constant for $z =$ constant. From figure 17 it will be clear that this is correct for $\zeta(r, 0)$ up to $r = 0.6$. It should be remarked that the top-disk vorticity $\zeta(r, 1)$ (not displayed) also shows agreement with the similarity value, but over a smaller interval of the radius. This is caused by the presence of a stagnation point at the top disk ($r = r_{st}$) where $\zeta(r, 1)$ changes sign.

Note the position of the computational coordinate $x = 0.5$ in figure 17. This shows the effect of the radial transformation (§3.2). Further note that the results for the fine grid $41 \times 41$ near $r = 0$ are significantly closer to the similarity solution than the results obtained with the $21 \times 21$ grid. The error in the latter vorticity results is about 10%. Richardson extrapolation reduces this error level to 1% (see §A.3).

A.2.3. *The case* $s = -0.8$ (figure 18). At $Ek = 0.01$ and $s = -0.8$ axial profiles of the tangential and the axial velocities are compared with the similarity results in figure 18. Again good agreement is obtained. The profiles at $r = 0.2233$ strongly suggest a Stewartson type of solution, although the Reynolds number ($Re^* = 100$) is not large enough to show this more rigorously. However, later experimental measurements have revealed that for strong counter-rotation and $Re^* = 500$–$1000$ the tangential velocity in the bulk virtually vanishes, while the radial velocity is negative and almost constant in the region between the boundary layers. This is completely in agreement with predictions by Stewartson (1953).

The dotted curve in figure 18 represents the tangential velocity at $r = 0.8881$, which shows an interior transition layer as predicted by Batchelor (1951). However, at this value of $r$ the similarity demands are not satisfied (see also §5.3). Nevertheless we may conclude that the rotating flow in the confined geometry at strong counter-rotation contains both Stewartson and Batchelor profiles, united together in one solution of the full partial differential equations.
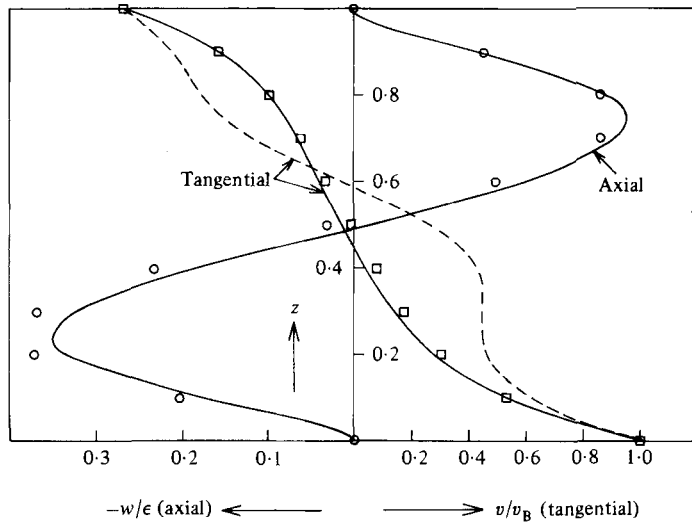
FIGURE 18. Comparison between numerical results for axial and azimuthal velocity; $s = -0.8$, $Ek = 0.01$, $Ro = 1.8$, $\epsilon = (Ek/Ro)^{\frac{1}{2}}$, $v_B = v$ at bottom disk: ——, similarity solution at $r = 0.2233$; □, ○, full partial differential equations (21 × 21 grid), $r = 0.2233$; ———, tangential-velocity profile at $r = 0.8881$ (21 × 21 grid).

## A.3. *Stagnation point*

In §5.4 the location $r_{st}$ of the stagnation point has been investigated. If we only consider the range $-1 < s < 0$ the stagnation point (if any) is located at the slower-rotating top disk. Consider figure 14, which shows the position $r_{st}$ of the stagnation point for various values of $s$ at $Ek = 0.01$. These results strongly suggest that $r_{st}$ will vanish at a certain value $s = s_{st}$:

$$s = s_{st} \Leftrightarrow r_{st} = 0. \qquad (A\ 7)$$

In fact figure 14 indicates that the vanishing of $r_{st}$ will take place with $(|s - s_{st}|)^{\frac{1}{2}}$ as $s \to s_{st}$.

Further support for this behaviour has been obtained in additional experimental and numerical work. The value $s = s_{st}$ is important since it characterizes the global flow structure in the meridional plane for a given $Ek$-number as follows:

$$s > s_{st} \Rightarrow \text{no stagnation point} \Rightarrow \text{one-cell structure},$$

$$-1 < s < s_{st} \Rightarrow \text{stagnation point at top disk } (r_{st} \neq 0) \Rightarrow \text{two-cell structure}.$$

At $Ek = 0.01$ the value of $s_{st}$ predicted by figure 14 is about $-0.12$. In the $\sigma$-range $-1 < \sigma < 0$ (slower-rotating bottom disk) the same numerical value is obtained. Hence the value of $s_{st}$ is not (or is only weakly) influenced by the sidewall. Lugt & Haussling (1973) reported transition from one- to two-cell structure at $Ek = 0.01$ for $\sigma = -0.11$. They investigated the geometry with an aspect ratio $\delta = 1$, and since the present aspect ratio is $0.07$ it follows that the transition value $s_{st}$ is independent of the aspect ratio $\delta$ for a wide regime of values. At the same time this implies that the disappearance of the stagnation point should be predictable by similarity considerations. To see this we consider the top-disk vorticity $\zeta(r, 1)$ when there is a stagnation point at that disk. For $r = r_{st}$ the top-disk vorticity vanishes and it also vanishes at the axis $r = 0$ by virtue of the boundary conditions (2.14). Hence

$$\zeta(0, 1) = \zeta(r_{st}, 1) = 0.$$

| $-s$ | $\epsilon\zeta(r,0)/r$ (bottom) | | $\epsilon\zeta(r,1)/r$ (top) | | $z_0$ = zero of $f(z)$ | |
|---|---|---|---|---|---|---|
| | Confined | Similarity | Confined | Similarity | Confined | Similarity |
| 0 | 0·461 | 0·509 | 0·154 | 0·085 | None | None |
| 0·03 | — | 0·488 | — | 0·036 | — | None |
| 0·07 | — | 0·446 | — | 0·022 | — | None |
| 0·10 | 0·406 | 0·421 | 0·051 | 0·018 | None | None |
| 0·15 | 0·367 | 0·387 | 0·013* | 0·007 | None | None |
| 0·20 | 0·336 | — | −0·002 | — | 0·93 | — |
| 0·22 | — | 0·351 | — | −0·010 | — | 0·76 |
| 0·25 | 0·312 | 0·338 | −0·016 | −0·018 | 0·74 | 0·68 |
| 0·30 | 0·293 | 0·318 | −0·029 | −0·032 | 0·66 | 0·61 |
| 0·50 | 0·236 | 0·258 | −0·076 | −0·083 | 0·54 | 0·51 |
| 0·80 | 0·183 | 0·200 | −0·129 | −0·143 | 0·52 | 0·49 |

TABLE 2

Now, as $s \to s_{st}$ we have $r_{st} \to 0$, which means that $\zeta(r, 1)$ must have a double zero at $r = 0$ in the limit $s \to s_{st}$. In other words

$$\zeta(0, 1) = \frac{\partial \zeta}{\partial r}(0, 1) = 0 \quad (s = s_{st}).$$

If the extra condition on the derivative is applied to the similarity representation (A 3) we find
$$f''(1) = 0 \quad (s = s_{st}). \tag{A 8}$$

This condition also follows from an argument based on streamlines. Consider the dividing streamline $\psi = 0$ in figure 9(a). It originates at the stagnation point $(r, z) = (r_{st}, 1)$ and it ends at the axis $(r, z) = (0, z_0)$, say. From (A 2) it then follows that $f(z_0) = 0$. Hence apart from the two double zeros at the disks, (A 5), the similarity function $f(z)$ has one (and only one) additional zero at $z = z_0$ when there is a two-cell structure. As $r_{st} \to 0$ the cell near the top disk shrinks in size and we must have $z_0 \to 1$. In the limit $f(z)$ has a triple zero at $z = 1$:

$$f(1) = f'(1) = f''(1) = 0 \quad \text{as } r_{st} \to 0.$$

The extra condition $f''(1) = 0$ is the same as before. This condition can be used to locate the transition value $s = s_{st}$ for a given $Ek$-number by means of the similarity hypothesis. At $Ek = 0\cdot01$ the similarity equations have been solved in the range $-1 < s < 0$ and the results are compared with those of the confined calculation – if available – in table 2. In this table $r = 0\cdot2233$ and $\epsilon = (Ek/Ro)^{\frac{1}{2}}$ ($Ek = 0\cdot01$, $Ro = 1 - s$). A bar (—) means that the case in question has not been calculated, while 'none' indicates that the similarity function $f(z)$, (A 2), does not vanish in the range $0 < z < 1$ between the disks.

From table 2 it is found that the top-disk vorticity vanishes at $s = s_{st} = -0\cdot18$, which should be compared with the experimental prediction $-0\cdot12$ at $Ek = 0\cdot01$. The relatively large difference between these results is likely to be due to radial effects not contained in the similarity hypothesis: it will be clear that a small second cell near $r = 0, z = 1$ is a non-uniformity in the flow field which requires additional terms in the representation (A 2). This may also be illustrated by the entry marked * in table 2. The corresponding value of this quantity at $r = 0\cdot0824$ was found to be $0\cdot008$ and this is significantly closer to the similarity value $0\cdot007$. This means that the region of validity of the similarity assumptions strongly depends on the distance $r_{st}$ from

the stagnation point to the axis. On the other hand the bottom-disk vorticity in table 2 shows good agreement between confined and similarity results for the full range of $s$-values. The 10 % difference is mainly due to numerical errors in the confined solution obtained with the $21 \times 21$ grid. To demonstrate that this 10 % error is of a numerical nature we compare (at $s = -0.3$) the bottom-disk vorticity quantity from table 2 for two grids, $21 \times 21$ and $41 \times 41$. These results are 0.293 and 0.309 respectively. Extrapolation yields 0.314 as compared with 0.318 according to the similarity solution. The error thus reduces to about 1 %. Further it is seen from table 2 that the zero $z_0$ of $f(z)$ tends to 1 as $s \rightarrow -0.18$ and that it tends to 0.5 for $s \rightarrow -1$, as it should by virtue of symmetry.

Calculations of a similar nature at other values of $Ek$ are planned for the near future.

Finally we consider the prediction of $s_{st}$ in the limit $Ek \rightarrow \infty$ ($Re^* \rightarrow 0$). In this limit (A 4) reduces to

$$g'' = 0, \quad \epsilon^2 f^{iv} = -2gg', \quad \epsilon^2 = Ek/Ro,$$

with boundary conditions (A 5). The solution is

$$\left. \begin{array}{c} (1-s)\,g(z) = 1 - (1-s)\,z, \\[2mm] \dfrac{60f(z)}{Re^*} = z^2(1-z)^2\,\{(s-1)\,z + (3+2s)\}. \end{array} \right\} \qquad \text{(A 9)}$$

Hence $f(z)$ has one and only one additional zero at

$$z_0 = \frac{3+2s}{1-s},$$

in this case. Putting $z_0 = 1$ we obtain in the limit $Re^* \rightarrow 0$

$$s_{st} = -\tfrac{2}{3}, \qquad \text{(A 10)}$$

while $z_0 = 0$ for $s = -\tfrac{3}{2} = \sigma_{st}^{-1}$, in agreement with the reciprocity principle obtained by interchanging the angular velocities of the two disks. The result (A 10) means that, in the limit considered 67 % counter-rotation is required before a stagnation point will appear.

Equation (A 9) gives the leading terms of a regular perturbation expansion about $Re^* = 0$. The procedure may be continued, but the labour becomes tedious. Instead of hand calculation we hope to do this by means of a computer, using formula manipulation, in the near future.

## REFERENCES

BATCHELOR, G. K. 1951 Note on a class of solutions of the Navier–Stokes equations representing steady rotationally-symmetric flow. *Q. J. Mech. Appl. Maths* **4**, 29–41.

BIEN, F. & PENNER, S. S. 1970 Velocity profiles in steady and unsteady rotating flows for a finite cylindrical geometry. *Phys. Fluids* **13**, 1665–1671.

DIJKSTRA, D. 1980 On the relation between adjacent inviscid cell type solutions to the rotating-disk equations. *J. Engng Maths* **14**, 133–154.

HOLODNIOK, M., KUBICEK, M. & HLAVAČEK, V. 1977 Computation of the flow between two rotating coaxial disks. *J. Fluid Mech.* **81**, 689–699.

HOLODNIOK, M., KUBICEK, M. & HLAVACEK, V. 1981 Computation of the flow between two rotating coaxial disks: multiplicity of steady-state solutions. *J. Fluid Mech.* **108**, 227–240.

LUGT, N. J. & HAUSSLING, H. J. 1973 Development of flow circulation in a rotating tank. *Acta Mech.* **18**, 255–272.

MELLOR, G. L., CHAPPLE, P. J. & STOKES, V. K. 1968 On the flow between a rotating and a stationary disk. *J. Fluid Mech.* **31**, 95–112.

NGUYEN, N. D., RIBAULT, J. P. & FLORENT, P. 1975 Multiple solutions for flow between coaxial disks. *J. Fluid Mech.* **68**, 369–388.

PAO, H. P. 1970 A numerical computation of a confined rotating flow. *Trans A.S.M.E.* E: *J. Appl. Mech.* **37**, 480–487.

PAO, H. P. 1972 Numerical solution of the Navier–Stokes equations for flows in the disk–cylinder system. *Phys. Fluids* **15**, 4–11.

PICHA, K. G. & ECKERT, E. R. G. 1958 Study of the air flow between coaxial disks rotating with arbitrary velocities in an open or enclosed space. In *Proc. 3rd U.S. Natl Congr. of Appl. Mech.*, pp. 791–798.

ROBERTS, S. M. & SHIPMAN, J. S. 1976 Computation of the flow between a rotating and a stationary disk. *J. Fluid Mech.* **73**, 53–63.

STEWARTSON, K. 1953 On the flow between two rotating coaxial disks. *Proc. Camb. Phil. Soc.* **49**, 333–341.

KÁRMÁN, T. VON 1921 Über laminare und turbulente Reibung. *Z. angew. Math. Mech.* **1**, 233–252.

ZANDBERGEN, P. J. 1979 New solutions of the Kármán problem for rotating flows. In *Lecture Notes in Mathematics*, vol. 771, pp. 563–581. Springer.

ZANDBERGEN, P. J. & DIJKSTRA, D. 1977 Non-unique solutions of the Navier–Stokes equations for the Kármán swirling flow. *J. Engng Maths* **11**, 167–188.